UNIVERSITÀ DEGLI
STUDI DI TRENTO

UNIVERSITÄT
TÜBINGEN

Laurea magistrale in Fisica

Studiengang Physik Diplom

Elaborato finale

Diplomarbeit

X-RAY INVESTIGATION OF THE COMPACT SOURCE XMMU J173203.3-344518

Relatori/Gutachter:

Prof. Dr. Andrea Santangelo
Prof. Giovanni Andrea Prodi

Laureando/Diplomand:

Silvia Simon

Correlatori/Betreuer:

Dmitry Klochkov
Gerd Pühlhofer

Anno Accademico 2011 - 2012

Wintersemester 2012 - 2013

Ai miei genitori

Hiermit wird bestätigt, dass die Diplomarbeit selbständig verfasst und keine anderen als die angegebenen Quellen und Hilfsmittel benutzt wurden.

Tübingen, den 23.01.2013

.....

SILVIA SIMON

Contents

List of Figures

List of Tables

Chapter 1

Introduction

After the discovery of the first radio pulsar by Jocelyn Bell and Antony Hewish in 1967, about 2000 neutron stars have been identified, with heterogeneous characteristics.
The vast majority of those stars have been identified as radio pulsars, whereas the detected radio-quiet X-ray emitting isolated neutron stars (XINSs) number only some tens [39].

To the population of XINSs belong anomalous X-ray pulsars (AXPs), soft gamma-ray repeaters (SGRs), central compact objects (CCOs) and X-ray dim isolated neutron stars (XDINSs).

CCOs are a group of fewer than 10 neutron stars found in the geometrical center of young supernova remnants (SNRs) emitting a thermal spectrum mainly in the X-ray wavebands. They are also characterized by a steady flux of the emission and the absence of pulsar wind nebula or non-thermal emission from the magnetosphere [49]. Pulsations were detected from four CCOs and the small spin-down periods indicates a very stable period of pulsation.

Far more radio pulsars than CCOs were discovered, but the for the disproportion in the detections is most likely not to be found exclusively in different birth rates of the two objects.

Depending on characteristics such as the strength of the emission, some categories of sources could be visible to our instruments only within a certain distance or even not at all. Moreover, also the evolution of the source must be taken into account, as a certain kind of emission may be produced by a source only during a resticted period of its life.

In fact, if we consider only those neutron stars found in the center of a SNR and at distances smaller than 5 kpc, we find 6 CCOs and 1 AXP, whereas there are only 14 radio pulsars [11]. CCOs must therefore be a quite common product of supernova explosions, yet we still know little about these objects and any further information is highly valuable in the characterization of the class and in the understanding of neutron star formation.

XMMU J173203.3-344518 is a new CCO, recently discovered in the center of the bright TeV emitting shell SNR HESS J1731-347. The complex was estimated to be probably located in the Scutum-Crux arm (~ 3.0 kpc) or the Norma arm (~ 4.5 kpc). Its radiation is consistent with at least an absorbed balckbody spectrum component with effective temperature $K_B T \sim 0.5$ keV.
No specific evidence for pulsation of the emission was given and no modulation of the flux was reported during a time span of three years.

It was not possible to incontrovertibly establish the nature of the object, because its characteristics are compatible with both AXP and CCO classes.
Further observations of the source were needed, in order to detect either pulsations or flux variations.
In fact, detection of pulsations would probably clarify the puzzle, as AXPs and CCOs have different typical pulsation periods and period derivatives.
On the other hand, detection of a significative flux variability would favour the AXP hypothesis.

Previous spectral analysis on the source spectrum had estimated the area of emission to be smaller than the surface of the neutron star. In fact, assuming a distance of 3.5 kpc the emission radius is about 2 km [1].
The combination of fast rotation of the star and the small emission area should result in a pulsation of the source.
In case of no detection of pulsations this anomaly needs to be considered.

In this work we analyzed a new observation of the source XMMU J173203.3-344518 proposed by Dr. D.Klochkov and Dr. G.Pühlhofer and carried out with the telescope XMM-Newton in March 2012.
Through spectral analysis, flux measurement and search for pulsations we tried to answer to the open questions about this enigmatic source.

After a brief description of the compact object physics and the neutron star panorama in section 2, we summarized the former analysis on the source XMMU J173203.3-344518 in section 3.
The motivation for a new observation of the source and the measurement informations are reported in section 3.2, whereas in section 4 the telescope characteristics are described.
Our analysis is reported in section 5 and our conclusions and outlook follow in section 6.

Chapter 2

Neutron Stars and CCOs

2.1 Introduction: compact objects

A star reaches the final stages of stellar evolution when the majority of its nuclear fuel is exhausted. When energy production ceases, the thermal pressure reduces and the star can no longer support itself against gravitational forces.
As a consequence, the star begins to collapse and a process begins, which can be explosive to a greater or lesser extent. This leads to the formation of a compact object, assuming that the star doesn't get completely wiped out [41].

Compact objects differ from normal stars principally due to very small size, high density and the lack of interior nuclear burning.
In such a dense structure, the thermal pressure is negligible and the star is either held up by the quantum degeneracy pressure, as in the case of white dwarfs and neutron stars, or just continues collapsing, which is the case of the black holes [41].

2.1.1 Degeneracy pressure

Degeneracy pressure arises in extraordinarily dense gases of fermions and is determined by quantum mechanical effects. Good examples of degeneracy pressure in astrophysics are white dwarfs and neutron stars, whose equations of state are governed predominantly by degenerate electron and neutron gases respectively.

Fermions in the interiors of a compact star are stacked very tightly and, as a result of their space confinement, they can assume only discrete values of energy. Furthermore, they interact with each other and must therefore be handled as one single quantum mechanical system.

According to the *Pauli exclusion principle* those fermions are not allowed to occupy the same quantum state, i.e. to simultaneously possess the same quantum numbers. A restricted number of fermion can therefore occupy a different level on the energy ladder of the system.
In non degenerate gases most of those energy levels are free, but in degenerate gases all the lower energy levels are occupied.

As a consequence, the degenerate region can not be compressed. A given degenerate fermion system defined over a determined volume struggles to accept other fermions from outside, because all the low energy levels of the system are full. A huge amount of energy would be needed to occupy the highest energy levels, the only ones which are empty.

This resistence to compression is identified as the so-called degeneracy pressure.

2.1.2 Formation of compact objects

White dwarfs are produced by the progressive contraction of a dying low-mass star.
The density growth increases the electron degeneracy pressure, which opposes to the contraction until until it stops and the star reaches a new equilibrium configuration.

Neutron stars, conversely, are generated in the violent explosion of a massive star (mass generally comprised between 8 and 25 $M_\odot$ [29]).
During the explosion event - also known as a supernova - the entire star collapses dramatically, regardless of the degeneracy pressure applied by the electrons, as the gravitational forces exceed the maximal pressure.

At this stage *neutronization* plays a fundamental role [41].
Further compression of the degenerate electron gas removes some of the possible quantum states, so electrons must occupy the high energy states left. The electron fermi energy therefore increases and when it exceeds 1.29 MeV (the mass difference between proton and neutron) protons and electrons are transformed into neutrons:

$$p^+ + e^- \longrightarrow n + \nu_e$$

The inverse process, known as *beta decay*,

$$n + \nu_e \longrightarrow p^+ + e^-$$

is for the same reasons unfavourable under these circumstances, as only very high energy states are still free and the production of an electron is not affordable.

As a consequence, neutrons replace gradually almost all of the protons and the neutron degeneracy pressure can hold up the star from further collapse. This generates a new stable configuration: the neutron star.

Neutrons exert degeneracy pressure at higher densities than electrons, because neutrons are associated with a shorter De Broglie wavelength and therefore only start to interact when they are much closer to one another [23].

The mass of a white dwarf cannot exceed the Chandrasekhar limit of 1.46 $M_\odot$. The radius is of the order of thousands of km.

Neutron stars have masses between about 1.4 and 3 $M_\odot$ and a radius of about 10 Km.

2.2 Pulsars

Fast axial rotation is a basic characteristic of neutron stars.

During the collapse of the parent star, the radius shirinks by several orders of magnitude. The conservation of the angular momentum transforms the mild axial rotation of the parent star into a very fast rotation of the neutron star.

Another important feature is the *high magnetic field*.

Particle plasma, such as is present in the interiors of the progenitor and in the neutron star, has a very high electrical conductivity. In the limit of superconductive plasma a phenomenon known as *magnetic flux freezing* [41] occurs.
As a consequence, the magnetic flux density increases as $B \propto r^{-2}$ during the supernova collapse and neutron stars achieve magnetic field strengths generally in the range 10^6 - 10^9 T (10^{10} - 10^{13} G).

The combination of these two characteristics means, that neutron stars are usually detectable as *pulsars*.
In fact, the strong magnetic field accelerates charges on the surface of the neutron star, which produces a beam of radiation departing from the magnetic poles. The magnetic axis is usually misaligned with the rotation axis, so the direction of the beam varies continuously. With favourable inclination angles of the pulsar, the beams might periodically cross our line of sight and be detected as a pulsed emission [5].

The period of this pulsation, furthermore, is always slowly decreasing, due to *magnetic braking*. The misalignment of the magnetic and rotational axis displays a gigantic varying dipole moment, as seen from large distances. The radiation of electromagnetic energy is supplied at the expense of the rotational energy [41].

Although neutron stars had already been predicted by Baade and Zwicky in early 1934,

their actual discovery was made only in 1967 by Antony Hewish and Jocelyn Bell.
They detcted a pulsating radio signal, with a very well defined period of 1.33 s.
In the following months, many other of these objects were discovered, all characterized by polarised radio emission with short regular periods. Between these, there were the pulsar in the vela supernova remnant and the one in the crab nebula, with a period of 33 ms.

It was than clear that the body of these pulsars was the neutron star predicted by Baade and Zwicky, as it was the only object compact enough to afford such a fast rotation.
The maximal rotation period a neutron star can have without being torn apart by the centrifugal forces is about a half millisecond [41]. At the present day no pulsar has been detected with a period smaller than 1.5 ms.

Pulsars associated with supernova remannts also represented the best evidence that neutron stars are born in supernova explosions.

2.3 Emission mechanisms

Although neutron stars were first detected only in the radio waveband, they can emit over a broad spectrum from radio to gamma-ray.

Right after their formation, neutron stars experience high temperatures on the order of 10^{11}-10^{12} K, which are quickly significantly reduced by neutrino losses.
In some hundreds of years the surface temperature stabilises around 10^6 K and stays in this order of magnitude for about 10-100 kyr [8][37][41].
The neutron star therefore radiates a *thermal spectrum* in X-rays for an extremely long part of its life. Thermal emission can arise from the entire surface or from the polar regions, which are likely to be hit by accelerated particles and thus be heated to a higher temperature [5].
Sometimes both high and low temperature components are present and a two-temperature thermal spectrum is displayed, as it has been observed for Geminga [45].

Other important emissions are *non-thermal* and are usually related to high energy charged particles accelerated in the magnetosphere [5].

The strong magnetic field produces a very dense magnetosphere around the pulsar. The induced electric field rips charged particles away from the surface of the star. These particles are mainly electrons, which enter in the magnetosphere and stream around the pulsar.

The pulsar drags the electrons of the magnetosphere with itself in its rotation, all with the

same angular velocity. However, this is only possible for particles contained in the so-called light cylinder (see figure 2.1 left), the limit at which electrons should travel at the speed of light to follow the rigid rotation of the pulsar [38][41].

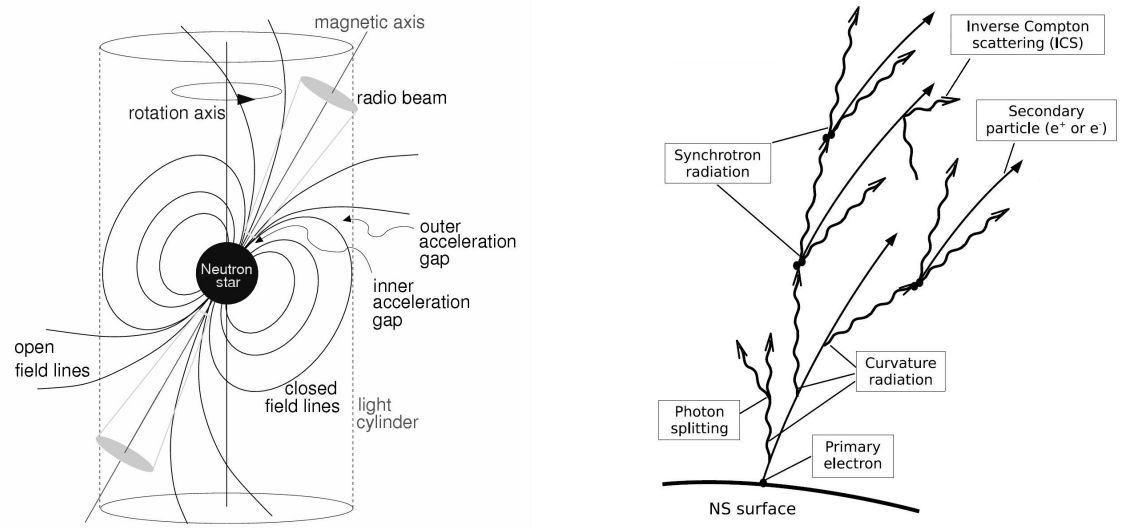

Figure 2.1: Left: Model of a pulsar. (Source: [41]) Right: The magnetosphere pair cascade. (Source: [44])

The magnetic field lines contained in the light cylinder are closed and the charges in those zones never leave the star.

The other magnetic field lines, though, are open and define two regions of the neutron star surface, the *polar caps*, from which electrons can stream out of the pulsar and escape to infinity [41].

The electrons enclosed in the field lines between the polar caps and the closed lines can stream out of the light cylinder, into the *wind zone* region surrounding the neutron star, in which they are still under the influence of the magnetic field. The termination shock of the relativistic particle flow can under some conditions be detected as a *pulsar wind nebula* [38].

The emissions from the pulsar's polar caps is considered to stem from *electron-positron pair cascades*.

An accelerated electron of the magnetosphere, escaping from the polar regions, quickly loses the component of its velocity perpendicular to the magnetic field, emitting *synchrotron radiation*. When the electron then streams along the magnetic field lines it also emits gamma rays. This is due to *curvature radiation* and *inverse Compton scattering* of the thermal X-rays from the surface [44].

These high energy photons interact with the strong magnetic fields and decay into electron-positron pairs, which undergo the same processes as the primary electron, producing at the end further pairs and activating a cascade [44].

Only if the magnetic field is strong enough can the gamma-ray photons generate electron-positron pairs, therefore the cascade process takes place only below a certain height and in relatively young stars.

Radio, infrared, X-ray and gamma-ray radiation can have very similar pulse profiles, but the striking difference lies in the brightness temperature of the radio emission, which can be even 10-15 orders of magnitude higher than in the other wavelenghts.

It is, in fact, also enormously higher than in any other radio sources and such a bright radiation must require some kind of coherent emission mechanism. Pulsar radio emission may be produced by bunches of particles radiating coherently but the details are poorly understood [41].

2.4 Normal radio pulsars and millisecond pulsars

Two fundamental characteristics of the pulsar detections are the period of the pulsation P and the time derivative of the period $\dot{P}$.

The pulsation period is, in fact, not stable and can be described by the relation:

$$\dot{\Omega} = -k\Omega^n$$

where Ω is the angular velocity and n the *braking index*, which depends on the braking mechanism. Assuming that the braking index is constant and integrating the relation above over the lifetime of the pulsar, the age τ of the star can be calculated:

$$\tau = \frac{\Omega^{-(n-1)}}{k(n-1)} = -\frac{\Omega}{(n-1)\dot{\Omega}} = \frac{P}{(n-1)\dot{P}}$$

Assuming that the only braking mechanism of the pulsar is the magnetic braking, the associated braking index is $n = 3$. Using this value we can estimate the *characteristic age* of the pulsar as $\tau = \frac{P}{2\dot{P}}$ [41].
Also the magnetic field strength on the neutron star surface can be estimated from the period and its derivative, by using the relation:

$$B = 3.2 \cdot 10^{19} \left(P\dot{P}\right)^{1/2} G$$

assuming a standard moment of inertia of the star $I = 10^{45} g\, cm^2$ [5].

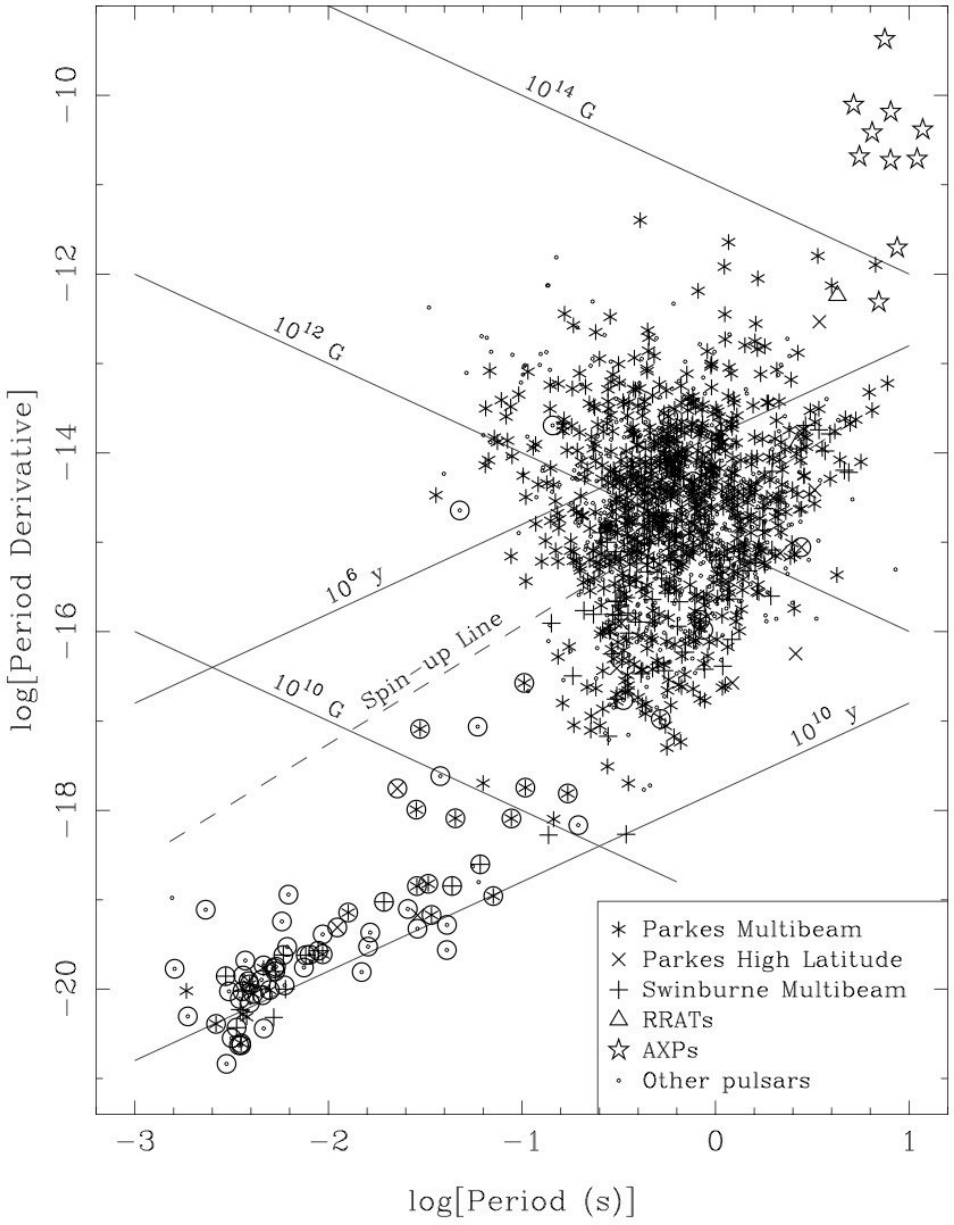

Figure 2.2: Distribution of the known pulsars in the P-P diagram, from the data described in Manchester et al. 2005. The enclosed circles represent the pulsars in a binary system. Lines of constant age and magnetic field are also shown. (Source: [5])

By comparing the period characteristics of the known pulsars, which are displayed in figure 2.2, two principal classes can be distinguished: the populous class of the normal radio pulsars, counting about 2000 members, which occupies the central region of the diagramm, and the millisecond pulsars class, at the bottom left. Their positions on the diagram suggest therefore different ages and magnetic field strengths for the two populations.

It is also interesting to observe that about 80% of millisecond pulsars belong to a binary system, as opposed to just 1% of the normal pulsars [5].

The interpretation of this discrepancy is that millisecond pulsars, which are older, were once normal pulsars in a binary system. After the companion star reached the final stages of the main sequence and became a red giant, exceeding the Roche-lobe, matter started streaming onto the neutron star. The matter accretion also transferred angular momentum, with a consequent decrease of the pulsar period. Despite the low magnetic fields, millisecond pulsars can still emit radio pulses thanks to the very high rotation frequency [41].

The cradle of millisecond pulsars is identificated in the X-ray binaries, which are binary systems composed of a main sequence star accreting onto a pulsar. In these systems the accretion is still very powerful and the main contribution to the emission comes from the hot accretion disc, radiating in X-ray waveband. Differently from normal pulsars, which are rotation-powered, X-ray binary systems are accretion-powered [41].

A binary system composed of two neutron stars is also possible, as PSR B1913+16 or the double pulsar system PSR J0737-3039 [41]. It is a wonderful environment for tests of general relativity, because both pulsars can be studied as clocks in a rotating (and therefore not inertial) frame of reference, in a strong gravitational and magnetic field.
Furthermore, the period of the orbit of the two pulsars changes, according to $-\frac{d\Omega}{dt} \propto \Omega^5$ [41], as expected for quadrupole emission of gravitational waves, and in some ten Myr the two stars are expected to coalesce [5].

There are no pulars on the bottom right of the diagram.
When a pulsar ages, its rotation slows down and the magnetic field decays. As a result the non-thermal emissions become too weak to detect and the star enters the pulsar graveyard.

Radio-quiet isolated neutron stars also belong to the normal radio pulsar family.
They are rotation-powered neutron stars which are visible as X-ray sources but not as radio pulsars. A possible hypothesis to explain this characteristic is that they are actually radio pulsars with emission beams directed away from the Earth [6]. Pulsar activity can manifest through nonthermal radiation from the magnetosphere, which can exceed the thermal X-ray surface radiation. In young radio-quiet pulsars non-thermal radiation from

a pulsar wind nebula surrounding the magnetosphere can also be detected.

On the other hand, there are also isolated neutron stars which are not rotation-powered, like X-ray dim isolated neutron stars (XDINs), magnetars and CCOs.
XDINs, also known as *the magnificent seven*, are isolated neutron stars emitting thermal soft X-rays, with a very faint counterpart in the optical waveband. The emission originates entirely from the cooling of the surface, as indicated by the pure blackbody spectrum. Pulsations with period $P \sim 3 - 12\,s$ were detected from six of the objects, with effective temperatures in the range $50 - 100\,eV$. XDINs have no binary companion, neither are they associated with a SNR.

2.5 Magnetars: SGRs and AXPs

The name *magnetar* is often used for neutron stars which are believed to possess enormous magnetic fields to the order of 10^{15} G [5] and can be spotted in figure 2.2 in the top right. Their peculiarity resides in the fact that the radiation is believed to be powered mainly by the decay of the magnetic field itself, instead of the rotational kinetic energy, as is the case of conventional radio pulsars. This is supported by the estimates of the spin-down luminosity, which is much smaller than the detected X-ray luminosity.

The term magnetar is ofted used to describe two classes of sources, which are sometimes difficult to distinguish between: anomalous X-ray pulsars (AXPs) and soft gamma ray repeaters (SGRs).

AXPs exhibit a quiescent soft X-ray emission, whose spectrum is usually a blackbody or a blackbody with powerlaw, with effective temperatures in the range $0.4 - 0.5\,keV$.
The emission pulsates with relatively long periods between 2 and 11.8 s [43].
The spin-down rates are of the order of $10^{-11}\,Hz \cdot s$, which corresponds to a very small characteristic age, of some kyr [5].

SGRs possess similar characteristics and occasionally emit soft gamma-ray bursts (E<100 keV) in addition to quiescent radiation.
These events last less than one second and are emitted in succession during the active periods of the SGR, which occur for some minutes in the time span of years.
Episodic bright giant flares of about 5 min with very high energy spectra were also observed [5].

To date 9 neutron stars are confirmed to be SGRs and 11 are AXPs [43]. SGRs and AXPs are believed to be young objects, as 8 of them are associated to supernova remnants and most of them are located in our galaxy, on the galactic plane.

A possible model which describes the observed behaviour of AXPs and SGRs is based on the instability of the neutron stars' surface.
According to the magnetar hypothesis, neutron stars with such a high magnetic field are quite rare and are probably born with a fast rotation period, which was later slowed down by the differential rotation and the magnetic braking.
Magnetic diffusion and dissipation heat the surface, which radiates X-rays [5].

The crust, stressed by the influence of such a high magnetic field, is in a critical state and the slightest perturbation can crack the outer layers, triggering crust quakes. The crack disturbes the magnetic fields and field oscillations can accelerate electrons in the magnetosphere to about 100 keV. Their energy is radiated in short bursts [5].

More profound ruptures of the magnetar's surface are responsible for the giant flares.

The relationship between the two families is not clear. AXP could be the natural evolution of a SGR, or equally they could simply be magnetars born with different characteristics.

2.6 Central Compact Objects (CCOs)

Soft X-ray sources found very close to the center of young SNR are usually referred to as Central Compact Objects (CCOs).
Their emission has a steady flux and no counterpart in the radio, infrared and optical waveband. The thermal spectrum is compatible with relatively high temperatures (0.2-0.5 keV) in comparison with other cooling NS and is characterized with an emitting area smaller than the neutron star surface.
The radius of the emitting area R is calculated from the flux F and the distance of the source D, which is expressed as

$$F = \frac{L}{4\pi D^2} = \sigma T^4 \frac{R^2}{D^2},$$

where the luminosity L is

$$L = \sigma T^4 4\pi R^2,$$

and σT^4 is the radiation energy density and $4\pi R^2$ the emission area.

No pulsar wind nebula is associated to CCOs.
Characteristic is also the lack of non-termal emission, which is a sign of magnetospheric activity, present in most of the young, energetic pulsars [11][39].

Due to the association with SNRs, CCOs are believed to be relatively young objects.
Although at the present time less than 10 objects were identified as CCOs [39] and the nature of this class is still not well understood, they must be a relatively common outcome of supernova explosion. In fact, of the compact objects discovered inside of a SNR within

a distance of 5 kpc from the solar system, 14 are radio pulsars, 6 CCOs and only 1 AXP [11].

Pulsations were detected for only four of these objects, confirming their neutron star nature.

Some characteristics of the observed CCOs are listed in table 2.1.

CCO	SNR	Age kyr	Distance kpc	Period	Upper limit fp %	Luminosity 10^{33} erg/s
1E 161348-5055	RCW103	2	3.3	6.67 h	12-50	1.1-80
1E 1207.4-5209	G296.5+10.0	7	2.2	424 ms	10	1.2
CXOU J185238.6+004020	Kes 79	7	7.1	105 ms	80	3
RX J0822.0-4300	Puppis A	3.7	2.2	112 ms	11	5
CXOU J232327.9+584843	Cas A	0.32	3.4	-	< 13	2
1WGA J1713.4-3949	G347.3-0.5	2	1.3	-	< 7	0.6
CXOU J085201.4-461753	Vela Jr. (G350.1-0.3)	1	1	-	< 7	0.25
CXOU J160103.1-513353	G330.2+1.0	>1	5	-	<40	1

Table 2.1: A list of the known CCOs. f_p is the upper limit on the pulsed fraction for a search down to 12 ms or smaller, see also section 5.3.8. (Sources: [49][5][11][35][25][52][7])

CCOs are considered as one class because their emission has the same characteristics. However, we are most probably dealing with two intrinsically different kinds of neutron stars, which appear to have the same observational characteristics: *weakly magnetized isolated neutron stars* and possibly *dormant magnetars* [11].

The CCO group is actually very heterogeneous. Apart from the general characteristics, most of the stars show peculiar features.

1E 1613: it was the first CCO to be discovered. Its pulsation period is extremely long, 6.67(3) hours, and the spectrum varies strongly depending on the phase. Although the long period could refer to the orbital period of a Low Mass X-ray Binary, 1E 1613 does not belong to a binary system, as is shown by the low luminosity and the purely thermal spectrum. Spectrum, luminosity, and long term variability are, on the other hand, well compatible with the AXP scenario. The compact object was therefore supposed to be a *braked magnetar*, a very peculiar magnetar, whose spinning had possibly been slowed down by the propeller effect on the material of a surrounding fallback disk [11].

1E 1207: a peculiarity of this object is the negligible period evolution. As a consequence, the characteristic age is three ordes of magnitude bigger than the SNR age.
A unique feature of 1E 1207 is the spectrum, which is thermal-like with 4 absorption features. These features are almost entirely responsible for the pulsation and occur at energies in harmonic ratio [11]. The peculiarity of the spectrum could be explained by cyclotron features in the plasma surrounding the star. Under this assumption the magnetic field is estimated to be of the order of 10^{11} G [11].

CXOU J1852: similarly to 1E 1207, it presents a very stable pulsation period, with a weak magnetic field. The incredible characteristic of this object is an enormous pulsed fraction of 80%.
This value of pulsed fraction is very difficult to explain, if the pulsation is produced by a small hot region rotating with the neutron star, because the magnetic field on the surface, which is supposed to be extremely low, can not produce a sufficient temperature anisotropy. Even with large magnetic fields a value larger than 35% is theorically not possible [11].

RX J0822: pulsations were detected also for RX J0822, with a very small spin-down rate and magnetic field, similarly to 1E 1207 and CXOU J1852 [25].

CXOU J2323: Cassiopeia A is the last supernova explosion to have occurred in our galaxy, therefore its Central Compact Object CXOU J2323 is supposed to be very young. The Spitzer telescope detected some fast moving features in the surrounding SNR, which could have been produced by a large flare of the CCO in 1953 [11], with a luminosity typical for the giant flare from SGRs. On the basis of this event, CXOU J2323 might be a dormant magnetar [11].

1E 1613 could be a very peculiar magnetar, whereas CXOU J2323 could be a magnetar in a particularly long quiescent phase. On the other hand, 1E1207, CXOU J1852 and the central source in Puppis A are certainly weak magnetic field isolated neutron stars [11].

Weakly magnetized INSs, also called *anti magnetars*, could be originated in similar circumstances as for the normal radio pulsars. In the case of a weakly magnetized INS, a slow birth rotation would have triggered a weak magnetic field, enabling the accretion of fallback material, which would have then extinguished the radio emission [11].
Considering the extraordinary properties of some of these objects, like 1E 1207 and CXOU J1852, it is still unclear if the X-ray emission originates from the surface of the hot neutron star or from the magnetosphere [11].

Chapter 3

The source XMMU J173203.3-344518 and a new measurement

3.1 The Supernova remnant HESS J1731-347

The sky surveys performed by the Cherenkov telescope H.E.S.S. (High Energy Stereoscopic System) led to the discovery of many of the 61 known galactic TeV γ-ray sources [66].
The identification of a counterpart in other wavebands for these objects is very important for understanding the emission mechanisms and therefore the nature of the source.
About a half of these objects are pulsar wind nebulae and young shell-like supernova remnants: in fact, their powerful shock waves can accelerate particles up to TeV energies, which emit high energy photons interacting with the ISM [33].

The TeV source HESS J1731-347 was discovered in the VHE Galactic plane survey by H.E.S.S.
A couterpart was found by Tian et al. (2008) [60] in archivial radio data collected by ATCA during the Southern Galactic Plane Survey and identified with the faint radio shell of the supernova remnant G353.6-0.7, whose structure matched closely the VHE emission.

Further measurements performed by the satellite ROSAT in 1993 in the band 1.0-2.4 keV showed an X-ray feature partially matching the SNR shell.

X-ray radiation from the shell is produced by synchrotron emission only, no thermal emission has been detected [60][30]. This suggests that the SNR belongs to the very small class of non-thermal shell-type supernova remnants with VHE emission [4], of which it presumably is the most luminous object [30].

The X-ray emission fits well within the 0.5° radio shell.
The western region of the SNR, closer to the Galactic plane, is probably covered by an

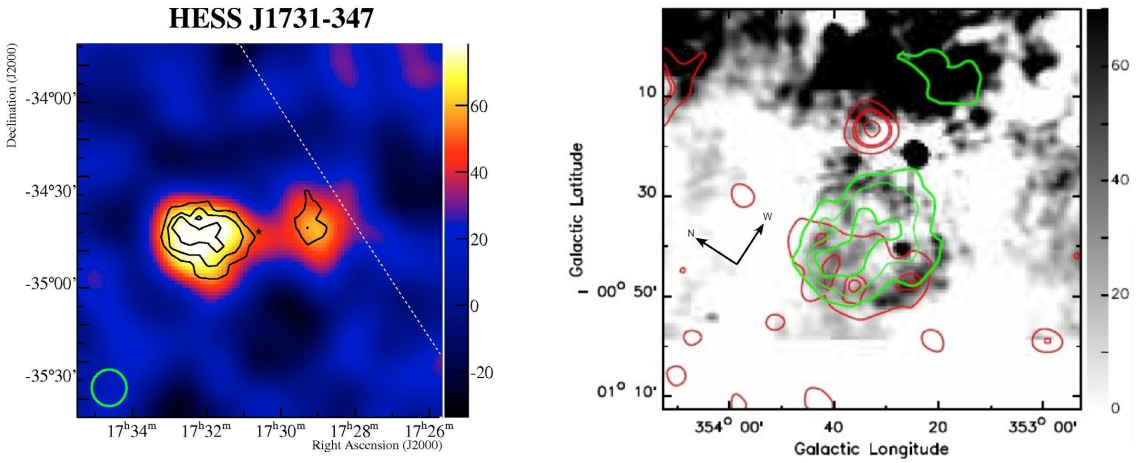

Figure 3.1: (Left: a first TeV-ray image of HESS J1731-347, discovered in the H.E.S.S. survey of the Galactic plane. Right: 1420 MHz radio continuum image of G353.6-0.7 with ROSAT image contours (red) and HESS J1731-347 image contours (green) overlaid. (Source: [31])

extended molecular cloud structure, which significantly absorbs mainly the emission in the X-ray wavebands [30][4].

The distance of the molecular cloud is 3.2 ± 0.8 kpc [60], estimated comparing the Doppler shift of ^{12}CO emission spectrum to a circular Galactic rotation model.
The cumulative absorption column of the atomic and molecular hydrogen, derived from the CO density and H_I observations, is similar to the one observed in X-rays. This suggests that the cloud is located in the foreground of the SNR. The distance estimate of 3.2 kpc sets therefore a lower limit to the distance of the X-ray source [30].

For such a distance, the diameter of the shell, which is $0.54(4)°$, has a lower limit of 30 pc [30].

Despite the large dimensions, the SNR is relatively young. Considering a shock speed of 3000 km s^{-1}, similar to that of other bright synchrotron emitting SNRs, the age is estimated to be around 2.5 kyr [30].

Supernova explosions are more likely to occur in the spiral arms of the Galaxy. Considering the structure of the Milky Way, as in figure 3.2, and the lower limit to the distance, HESS J1731-347 is probably located either within the Scutum-Crux arm ($\approx$ 3.0 kpc) or the Norma-Cygnus arm ($\approx$ 4.5 kpc) [30].

A location in the Sagittarius-Carina arm ($\approx$ 12 kpc) is highly unlikely: at such distances the TeV luminosity of the SNR would be exceedingly high and the diameter larger than 100 pc, whereas the other TeV shell SNRs have diameter smaller than 30 pc [30].

Follow-up measurements could detect an unresolved compact X-ray source located very

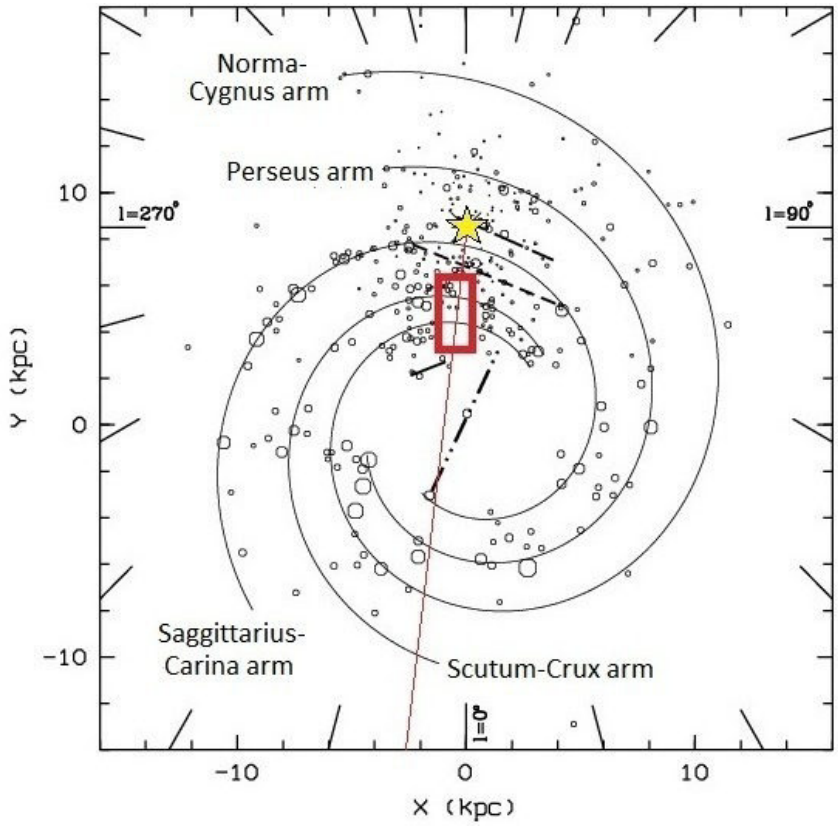

Figure 3.2: Milky way: the yellow star is the sun, the red line the direction of HESS J1731-347 and the red box the location region. (Source: [51])

close to the geometrical center of the SNR: XMMU J173203.3-344518 [1], as can be seen in figure 3.3. The source has no counterpart in any other wavelength.

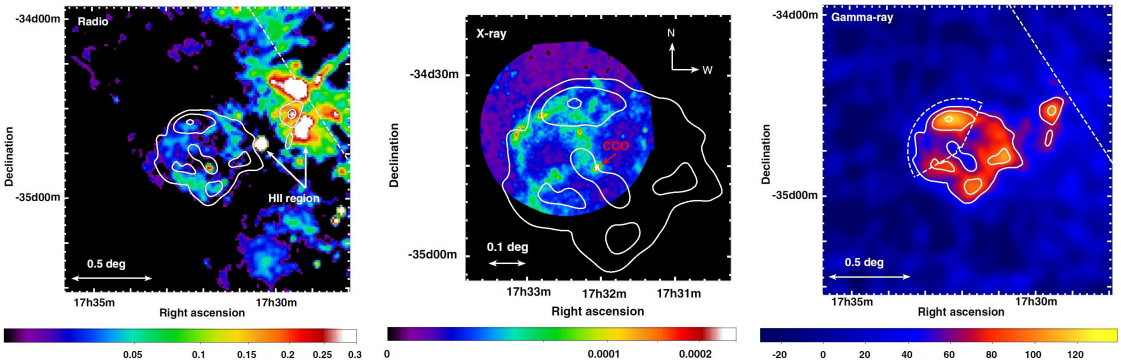

Figure 3.3: Radio, X-ray and gamma-ray view of the HESS J1731.347 region. The possible CCO candidate can be seen in the X-ray panel. (Source: [30])

3.1.1 The compact source XMMU J173203.3-344518

The unresolved central object emits only in the X-ray waveband and the former analysis refer to the X-ray datasets reported in table 3.1.

Satellite	Instr./mode	Obs. ID	Date (UT)	Exposure (ks)	Energy range (keV)	Time res.
Suzaku	XIS/Normal	401099010	23 Feb 2007	40.6	0.2-10	8 s
XMM	pn+MOS/FF	0405680201	21 Mar 2007	25.4	0.15-12	73.4 ms
Chandra*	ACIS-I/TE/VF	9139	28 Apr 2008	29.6	0.2-10	3.2 s
Swift	XRT/PC	00037740001	04 Feb 2009	1.4	0.2-10	2.5 s
Swift	XRT/PC	00037740002	15 Mar 2009	1.4	0.2-10	2.5 s
Chandra	ACIS-S3/CC/F	11234	18 May 2010	39.9	0.2-10	2.85 ms

Table 3.1: List of observations of the compact source XMMU J173203.3-344518. The first Chandra measurement (c) is strongly affected by photon pileup. (Source: [27][28][9][24])

The analysis results of these datasets were presented in different papers.
Various models were used in the spectral analysis of the source, in order to understand its emission properties.
A blackbody emission is typical for CCO and AXP, where photons are most likely radiated from the hot surface.
A power law model refers to non-thermal emissions, which could be produced in the star magnetosphere or in a possible pulsar wind nebula.
A blackbody plus powerlaw emission is also possible, if both above mentioned scenarios are combined.

A two-blackbody spectrum model could describe the thermal emission from a hot star surface with restricted hot regions.

In what follows we summarize main previous results.

Acero et al. (2009) [1]:
The best fit for the XMM-Newton dataset is an *absorbed blackbody* with temperature $k_BT = 0.5\,keV$ and there is no strong evidence for a powerlaw tail component.
The normalisation of the spectrum fixes the proportion between emission radius and distance of the source, yielding an emission radius of 2 km, if the source is located at 3.5 kpc. It also provides a constraint for the source distance as smaller than 20 kpc, the distance at which the emission originates from the whole neutron star surface.
The flux is constant and there is no evidence of pulsations.
The position of the source in the geometrical centrum of the SNR, the purely thermal spectrum and the lack of variability are all characteristic of a possible CCO.

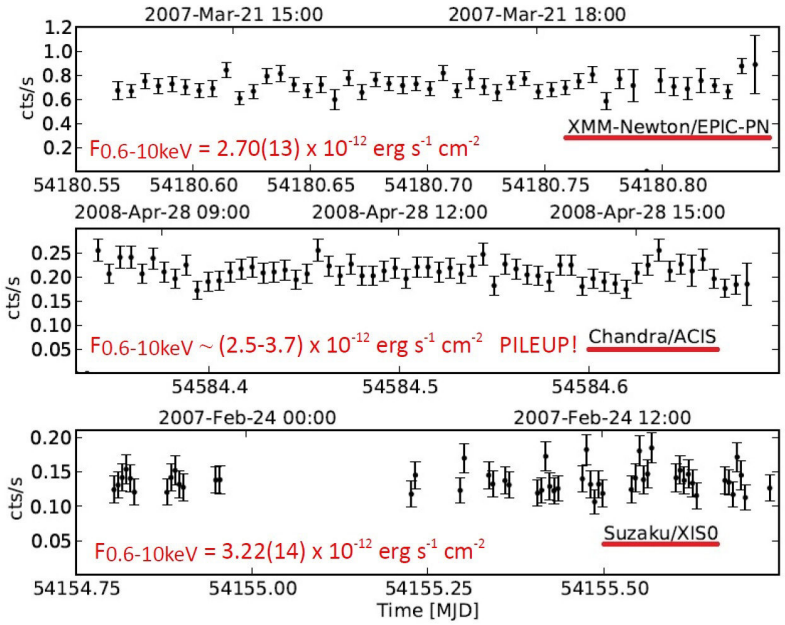

Figure 3.4: Light curves of the source XMMU J173203.3-344518 in different datasets: the flux is steady, there is no sign of variability. (Sources: [39])

Halpern et al. (2010a) [27]:
Powerlaw fits to the source spectra of Suzaku and XMM-Newton have too steep slopes.
Better fits are obtained with the *blackbody* spectrum, with temperature $k_BT = 0.5\,keV$, and *two-blackbody* spectrum. The obtained temperatures are typical of both CCOs and AXPs.
Suzaku, XMM-Newton and the Chandra (2008) observation agree to within 20% in flux. Swift short observations were aimed at the detection of a possible variability, which is the distinctive characteristic of the magnetars. Such activity was not registerd in the time

span of two years.
Timing analysis of XMM-Newton revealed marginal evidence for a period of 1.010441(6) s, modulated with a 10% pulsed fraction. The 2.7% chance probability for a search down to 150ms is, however, too weak to determine a sure detection.

Tian et al. (2010) [61]:
Best fits on Suzaku and XMM-Newton data are obtained with combined models: *blackbody+powerlaw* and *two-blackbody*. Powerlaw yields too steep a spectrum, not characteristic for a possible pulsar wind nebula.
The lack of flares and the low brightness favours the hypothesis of AXP, rather than SGR. The magnetar scenario was however not confirmed, because no pulsations were detected.

Halpern et al. (2010b) [28]:
Only marginal evidence for pulsation was found in XMM-Newton data and the best fit was obtained with a *two-blackbody*.
No pulsations were identified in the new Chandra (2010) dataset down to 10 ms: the 95% confidence upper limit on the pulsed fraction of a sinusoidal signal is 8.6%.
The two-blackbody model fits well also with the new spectrum. The flux of Chandra (2010) in the band 0.5-10 keV is identical to the one obtained with XMM-Newton, therefore the CCO scenario is more likely.

Bamba et al. (2012) [4]:
Absorbed blackbody and powerlaw fits are statistically unacceptable for Suzaku data, therefore the spectrum must have a multicomponent emission. Two-blackbody, blackbody+powerlaw and blackbody with contamination from the SNR emission models fit the spectrum well.

3.2 A new observation of XMMU J173203.3-344518

Although previous analysis of the spectrum of the source XMMU J173203.3-344518 had confirmed at least one blackbody component with temperature $k_BT = 0.5\,keV$ and the flux had proven to be constant over a time span of about three years, no sure conclusion had been achieved in the measurement of a possible pulsation.

In order to better characterize the nature of XMMU J173203.3-344518 new investigations were needed.
A new high time resolution observation of the compact source XMMU J173203.3-344518 was performed by the XMM-Newton telescope, at the instance of D.Klochkov and G.Pühlhofer [39].

Satellite	Instrument/mode	Observation ID	Date (UT)	Exposure (ks)	Time resolution
XMM-Newton	pn+MOS/TI	0673930101	2 Mar 2012	23	0.03 ms

Table 3.2: The new XMM-Newton measurement of the compact source XMMU J173203.3-344518

The telescope was operated in *timing mode*, which ensured a time resolution of the EPIC pn camera of ~ 0.03 ms. Analysis on previous measurements of the source could be performed only down to 10 ms (see time resolutions in table 3.1) and a better resolution allowed a more complete inspection of the temporal behaviour of the source.

The XMM-telescope was chosen not only for the competitive time resolution, but also for the high sensitivity in comparison also with Chandra, offered by the effective area and the long target visibility (see chapter 4.1 and table 4.2 for a comparison with other telescopes). The 20 ks exposure time ensured enough statistic to perform period search also in restricted energy ranges, in order to detect possible pulsations from different energy bands.

In this work spectral and time analysis of this dataset is performed.

Chapter 4

The XMM-Newton Telescope

The X-ray Multi-Mirror Telescope (XMM-Newton) is an X-ray observatory of the European Space Agency (ESA).

It was put into orbit in December 1999 by means of an Ariane 5 rocket and the mission was planned to end within 2 years, but the large success has permitted the extension of the mission at least until 31 December 2014, although the satellite can possibly operate for a longer time [12].

XMM-Newton, shown in figure 4.1, can detect photons from two windows of the electromagnetic spectrum: X-ray and optical-UV.

The **X-ray window** is covered by three Wolter type-1 telescopes, connected with different kinds of detectors: three EPIC European Photon Imaging Cameras cameras (EPIC) and two Reflection Grating Spectrometers (RGS) [22]. More specifically, the EPIC cameras consist of one EPIC pn camera and two EPIC MOS cameras and can detect photons from 0.15 to 12 keV.

The **optical-UV window** is covered by the so called optical monitor, a 30-cm telescope with a Micro-Channel Plate (MCP) detector. The OM can detect photons from 180 to 600 nm [22].

The photons are collected on the left, where the mirror modules focus them to che right side of the telescope. On the right, the focal plane hosts the detectors: the two MOS cameras, cooled down by horn radiators, and the pn camera, surrounded by the two RGS. Each EPIC MOS camera shares the incoming light from the mirror module with an RGS. The optical monitor can be spotted just behind the lower mirror module [22].

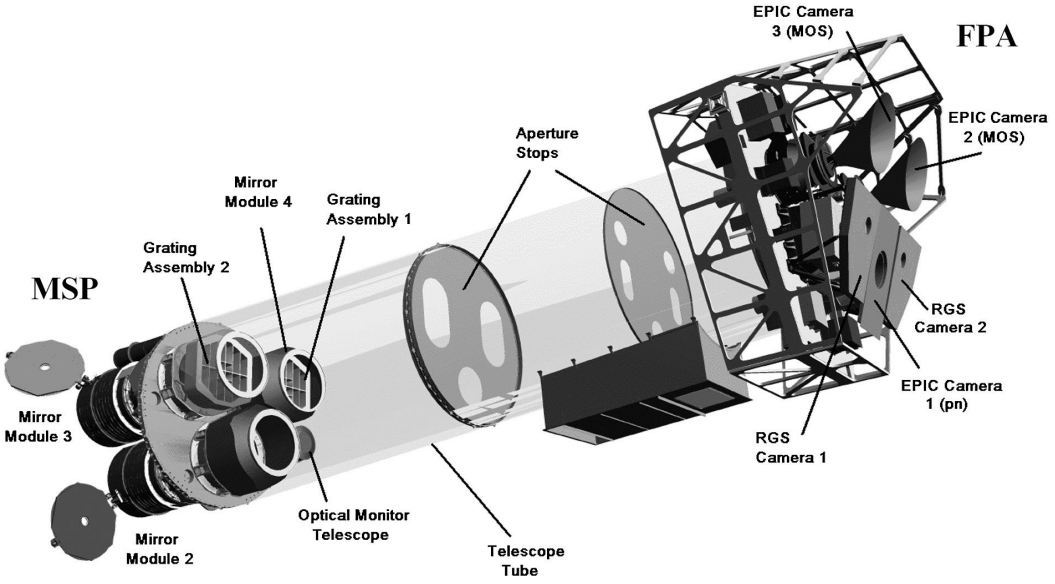

Figure 4.1: The structure of the telescope. (Source: [57])

The XMM-Newton Telescope carries onboard another instrument, the EPIC Radiation Monitor (ERM), which registers information about the particle irradiation, in order to avoid possible damage of the other instruments due to radiative belts and solar flares.

4.1 General features

The main features and strengths of XMM-Newton are a very high sensitivity and a high spectal and timing resolution [22].

1. **High sensitivity** is achieved via three outstanding characteristics of the telescope:
   - ***large effetive area:*** the X-ray telescopes mounted on the XMM-Newton telescope have the largest effective area of any operating focussing telescope. The total geometric effective area is $4650\,cm^2$ @1.5 keV.
   - ***good angular resolution:*** the 58 thin nested mirror shells in each X-ray telescope allow a PSF with a FWHM on the order of 6" and a HEW of ca. 15" (width at which 50% of the total energy is encircled) to be achieved.
   - ***long continuous target visibility:*** the XMM-Telescope travels on a highly elliptical orbit around the Earth; although no science observation is possible below $46000\,Km$ (at the apogee), one same target can be measured continuously for up to $40\,h$. This is also a necessary feature for source variability analysis.
2. **High spectral and timing resolution**

- ***spectral resolution:*** high-resolution spectroscopy is achieved with the RGS, with a resolving power $E/\Delta E \sim 200$-800, whereas the EPIC cameras offer a medium-resolution spectroscopy with $E/\Delta E \sim 20$-50.
- ***timing resolution:*** depending on the science mode, the EPIC cameras can offer timing resolution down to $0.03\,ms$ (or $7\,\mu s$ in burst mode).

3. Simultaneous operation of all science instruments

The instruments can be operated simultaneously and independently, so there are no constrains on the start and end time of the observations. Moreover, X-ray data can be compared to optical/UV data, which can identify possible counterparts of the observed X-ray sources.

The specific characteristics of the XMM-Newton telescope are summarized in table 4.1.

Table 4.1: XMM-Newton characteristics. (Source: [22])

	EPIC MOS	EPIC pn	RGS	OM
Bandpass	0.15 - 12 keV	0.15 - 12 keV	0.35 - 2.5 keV	180 - 600 nm
Visibility	5 - 135 ks	5 - 135 ks	5 - 135 ks	5 - 145 ks
Sensitivity	$\sim 10^{-14}$ *(a)*	$\sim 10^{-14}$ *(a)*	$\sim 8 \cdot 10^{-5}$ *(b)*	20.7 mag *(c)*
FOV	30'	30'	~5'	17'
PSF (FWHM/HEW)	5"/14"	6"/15"	N/A	1.4"/2.0"
Pixl size	40 μm (1.1")	150 μm (4.1")	81 μm (9x10^{-3}Å)	0.476513"
Time resolution *(d)*	1.75 ms	0.003 ms	0.6 s	0.5 s
Spectral resolution *(e)*	$\sim$ 70 eV	$\sim$ 80 eV	0.04/0.025 Å *(f)*	350 *(g)*

(a) In the range 0.15 - 12 keV, in units of erg s^{-1} cm^{-2}.
(b) O VII 0.57 keV line flux in photons cm^{-2} s^{-1}, for an integration time of 10 ks.
(c) 5-σ detection of an A0 star in 1000 s.
(d) In fast data aquisition mode.
(e) At 1 keV energy. At 6.4 keV, the energy resolution of both cameras is cs. 150 eV.
(f) In -1. and -2. order respectively.
(g) Resolving power ($\lambda/\Delta\lambda$) with UV and optical grism.

4.1.1 Comparison of XMM-Newton with other X-ray satellites

XMM-Newton Telescope of ESA is quite similar to Chandra, another X-ray telescope which was put on orbit by NASA just few months before. Together with the Suzaku telescope, they present extremely enhanced characteristics in comparison to their predecessors ASCA, ROSAT and RXTE. Table 4.2 offers a comparison of the main characteristics of the X-ray satellites.

Table 4.2: Comparison of XMM-Newton with other X-ray satellites. (Source: [22])

	Mirror PSF FWHM [arcsec]	Energy range [keV]	Area @ 1keV[(a)] [cm^2]	Visibility [hr]	Energy resolution @ 1keV [eV]
XMM	6	0.15 - 12	4650	36.7[(b)]	4
Chandra	0.2	0.1 - 10	555	44.4[(b)]	1
ROSAT	3.5	0.1 - 2.4	400	1.3[(c)]	500
ASCA	73	0.5 - 10	350	0.9[(c)]	100
Suzaku	-	0.2 - 600	1760	0.72[(c)]	50
RXTE	-	2 - 250	-	1[(c)]	-
Swift	8.8	0.2 - 10	133.5	∼0.8[(c)]	70

(a) Mirror effective area

(b) Orbital visibility outside of the particle-radiation dominated zone.

(c) Low orbit with Earth pccultation.

The characteristics of XMM-Newton and Chandra are quite complementary, as the first has a bigger collective area, while the second offers a better imaging quality. But the main difference is that the detectors mounted on XMM can be operated simultaneously and in different detecting modes without affecting the measurements one of the others [22].

4.2 The mirror modules

The mirror modules serve to focus of the incoming X-ray photons.

Optical photons are usually brought to convergence by means of the refraction of lenses or the reflection of mirrors at incidence angles of $\sim 90°$.
Both of these methods fail with high energy photons as the X-rays.

Lenses can't deflect X-ray photons enough to allow focussing, because the refractive index at such energies is approximately 1 for every material. Moreover, X-ray photons are strongly absorbed by the lense itself.
Mirrors can't reflect perpedicularly incident X-ray photons, which penetrate strongly in the medium or are absorbed [2].

A clever way to focus X-rays was found in the year 1952 by Hans Wolter, which exploited the principle of *total reflection* (figure 4.2).
X-rays in metals have a refractive index slightly smaller than 1, therefore metals are for these wavelenghts optically thinner than air or vacuum. If the high energy photons fall on a metal mirror under the condition of *grazing incidence*, i.e. with an incidence angle higher than the Brewster's angle ($\theta_B = \arcsin n_{mirror}$), then the entire beam is reflected [2].

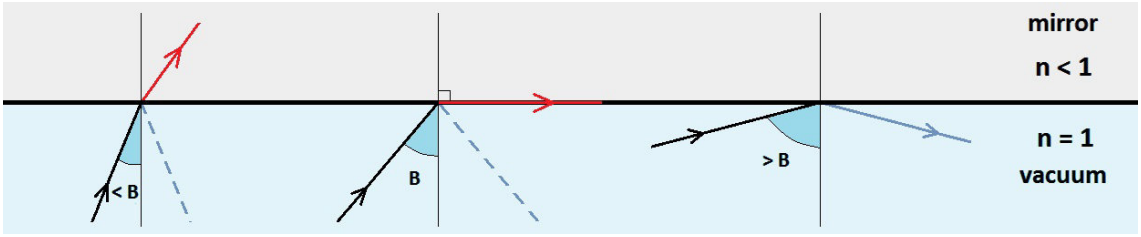

Figure 4.2: Left: at small incidence angles there is no reflection and the beam is completely transmitted or absorbed. Center: at the Brewster's angle the beam is still completely transmitted and deflected parallel to the mirror surface. Right: at higher angles the beam is completely reflected.

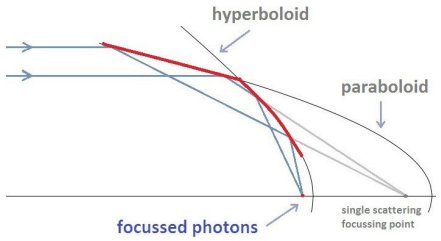

The Wolter telescope type-1 consists of a parabolic mirror and a confocal and coaxial hyperbolic mirror. The XMM-Newton carries onboard three mirror modules, each module consisting of 58 Wolter type-1 mirrors of gold-coated nickel, nested in a coaxial and confocal arrangement. This configuration collects only those photons, which enter the telescope with a grazing angle smaller than 30'. The very shallow grazing angle ensures a good reflectivity also at high energies, thus providing a large effective area [21].

Each of the three mirror assemblies (in figure 4.3) is composed of:

- **the mirror assembly door** to protect the optics during high background peiods;
- **an entrance baffle** which provides visible straylight suppression at angles larger than 47°;
- **an X-ray baffle** consisting of two sieve plates each with 58 annular apertures, located in front of the mirror systems. They act as collimators and block single-reflection photons;
- **the Mirror Module**
- **an electron deflector** which produces a circumferential magnetic field and diverts soft electrons reflected by the mirrors;
- **RGA** a Reflection Grating Array is carried by two of the three mirror assemblies [21].

The focal length of the mirror modules is $7.5\,m$. The photons focussed by the mirror assembly without RGA converge unobstructed on the focal plane in the EPIC pn camera.

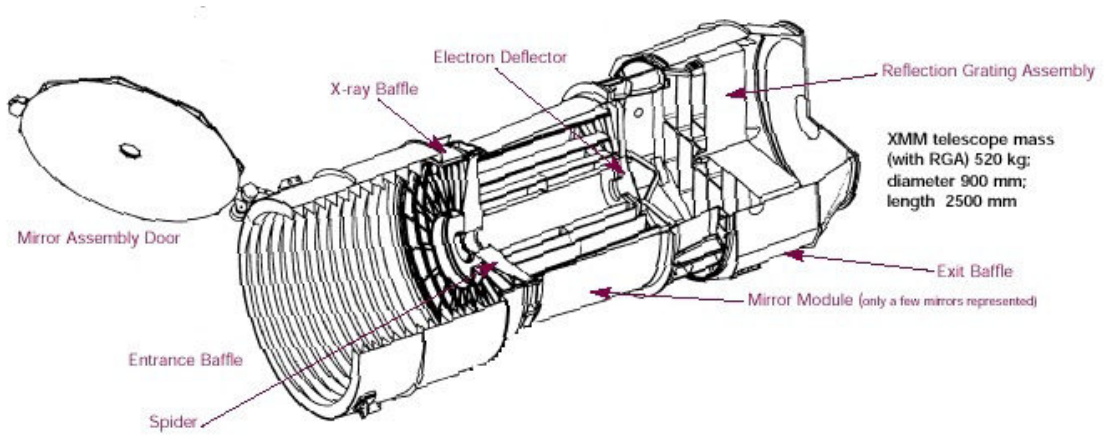

Figure 4.3: The mirror assembly. (Source: [21])

The RGA mounted on the other two mirror assemblies focuses 44% of the photons at the primary focus, where the two EPIC MOS cameras are placed, and 40% of the photons are dispersed towards the two Reflection Grating Spectrometer, at the secondary focus. The remaining 6% of the photons are lost.

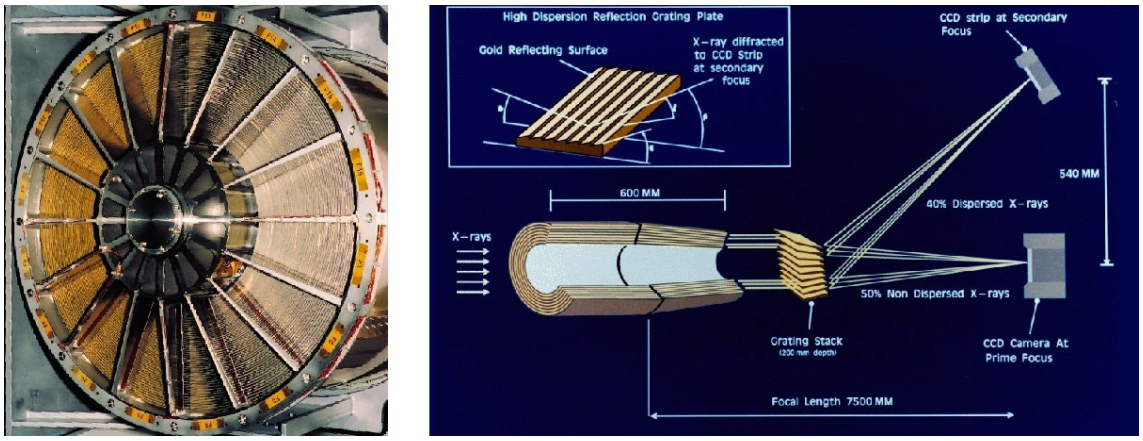

Figure 4.4: Left: one of the mirror modules with the X-ray baffle (radius of about 35 cm). Right: the Reflection Grating Array (RGA) spilts the photons into two beams. (Source: [21])

4.3 The EPIC cameras

On the XMM-Telescope are mounted the three EPIC cameras: one EPIC pn and two EPIC MOS (Metal Oxyde Semiconductor).
High sensitive imaging observations in the energy range of 0.15-12 keV can be achieved with the EPIC cameras over a FOV of 30', with a relatively good angular and spectral resolution (see paragraph 4.1) [22].

The EPIC cameras are sets of CCDs.

A charge-coupled device (CCD) is an integrated circuit carved on a doped silicon substrate. It is divided into a grid of elements called pixels, which collect the incident photons.
When a photon strikes a pixel, it is absorbed and a primary electron is released, due to the photoelectric effect. Secondary ionisation by the primary electron then produces other electrons in proportion to the former photon energy.
The photon energy can therefore be measured from the total charge present in the pixel, assuming that it did not collect multiple photons.
At the end of the exposure time, the electrons are shifted by means of electric fields along the CCD towards the end of the array, where they are read out [42].

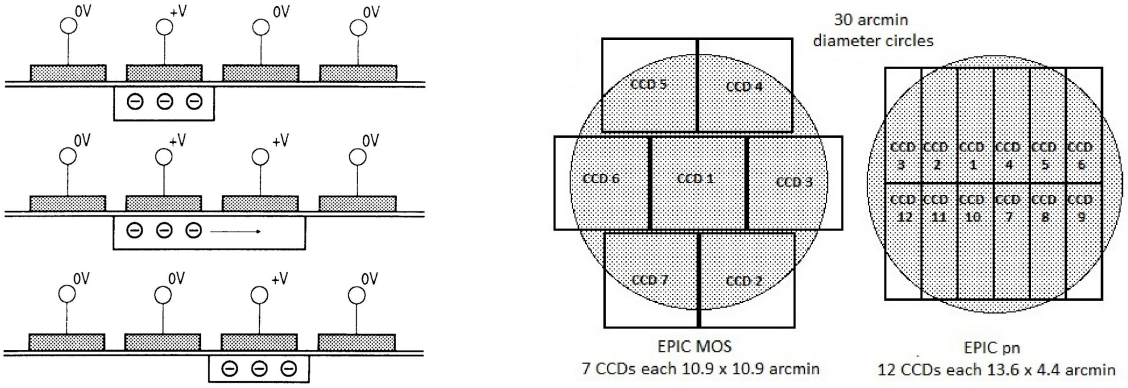

Figure 4.5: Left: How the charges are transferred in a CCD (Source: pixcellent.com). Right: The schematic layout of the CCDs of the EPIC cameras. The 30' diameter circles deline the FOV (Source: [22]).

Besides imaging, the energy resolution of each pixel of the EPIC CCDs also allows simultaneous non-dispersive spectroscopy.
Every scientific observation produces a so-called event list: in this file each photon detection occupies one line, where position, arrival time, energy of the photon and other additional attributes are specified [21].

MOS and pn cameras are different under many aspects, like geometry, readout modes and times, illumination, etc.

4.3.1 The EPIC MOS cameras

There are two MOS cameras on the XMM Newton, which are mounted on the focal plane orthogonally to each other.

As we can see in picture 4.6, each camera is composed of seven independent front-illuminated CCD chips. The CCDs slightly overlap each other, in order to follow the focal plane curvature and to minimize the gap regions on their edges.
Some 300 microns-wide dead regions could not be avoided, but those areas are covered by the other MOS camera, which is rotated by 90°.

Each CCD has 600x600 pixels of 40 micron (1.1 arcsec) square. The mirror PSF with HEW of 15 arcsec is covered by about 15 pixels [21].

On the 9th March 2005 a micrometeorite probably impacted with the telescope optics and some debris were scattered onto the focal plane, damaging the CCD6 of the MOS1 camera. The CCD6 was from that point turned off, since all pixels were returning just signal at saturation level [17]. The impact caused also a new hot column in CCD1, very close to the boresight [13].

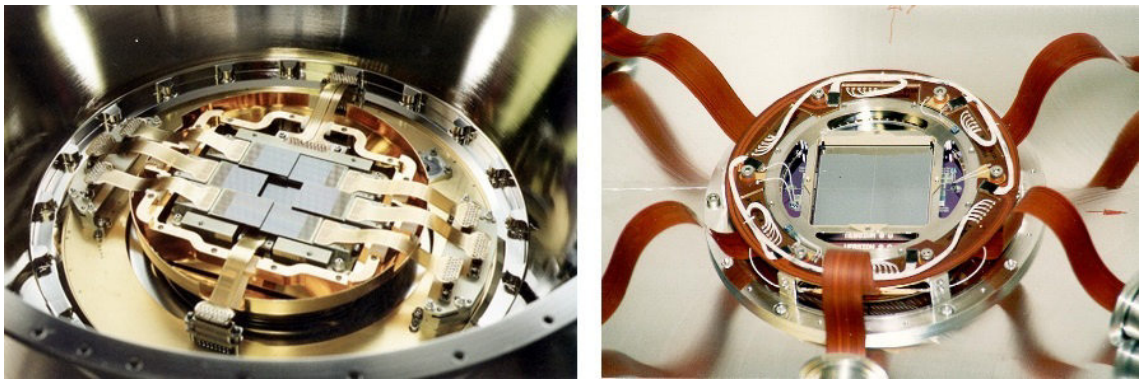

Figure 4.6: Left: one of the EPIC MOS cameras. Each CCD measures 2.5x2.5 cm. Right: the EPIC pn camera. Each CCD measures 1x3 cm. (Source: [21])

4.3.2 The EPIC pn camera

The pn camera consists of a monolithic silicon wafer with 12 back-illuminated CCD chips integrated.

The optical axis for the pn detector is not centered exactly in the middle of the CCD array, but slightly offset, so that more than 90% of the photons from an on axis point source are collected by one CCD (the CCD4).

The CCDs have 200x64 pixels of 150 microns (4.1 arcsec) square. The mirror PSF with HEW of 15 arcsec is here covered by about 4 pixels. The angular resolution of both kinds

of EPIC cameras are therefore determined by the mirror modules [21].

4.4 Science modes of the EPIC cameras

The EPIC cameras can be operated in different readout modes. For the MOS camera the 6 outer CCDs are always operated in standard imaging mode, while only the readout mode of the inner CCD can be changed.
The possible science modes of the EPIC cameras are:

full frame all pixels are read out and the entire FOV is covered. An ***extended full frame*** mode is also available for the pn camera, in which the image collection time is longer than in the normal full frame mode.

large window only a part of the pixels is read out

MOS: the inner CCD is active only in a central 300x300 pixel square of the total 600x600 pixel region;

pn: all 12 CCDs are read out, but only in their inner half part.

small window

MOS: the inner CCD is active only in a central 100x100 pixel square;

pn: only a part of the CCD4 is operating.

timing

MOS: the inner CCD images only in the x-dimension because the y-dimension is collapsed into one single pixel; the succeeding recordings, read out at high speed, are placed in a row, so that the result is a stripe;

pn: the CCD4 records one-dimensional data, such as the inner CCD of the MOS cameras.

burst (pn only) similar to the timing mode, it offers an outstanding time resolution of $7\,\mu s$, but is affected by a very low duty cycle (3%) [22].

The different modes can be chosen depending on the type of the object to be observed: whether we are dealng with a point-source or an extended source, a bright source or a faint source.
The choice of the science mode must also assure that some unpleasant effects are avoided, like too high an amount of out-of-time events or a high flux, which could lead to photon pile-up.

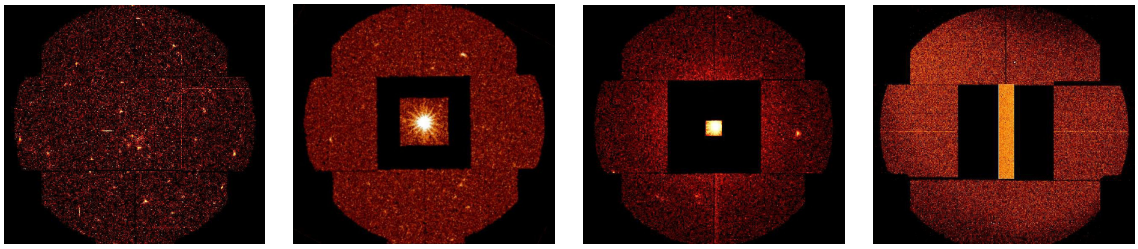

(a) *MOS - full frame (time resolution: 2.6 s).*
(b) *MOS - large window (time resolution: 0.9 s).*
(c) *MOS - small window (time resolution: 0.3 s).*
(d) *MOS - timing (time res.: 1.75ms).*

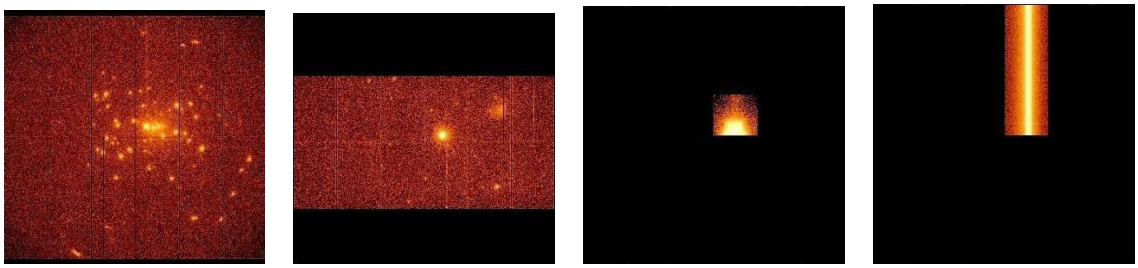

(e) *pn - full frame (time res.: 73.4ms).*
(f) *pn - large window (time res.: 47.7ms).*
(g) *pn - small window (time res.: 5.7ms).*
(h) *pn - timing (time res.: 0.03ms).*

Figure 4.7: Active areas of the MOS (above) and pn (below) CCDs depending on the science mode. (Source: [22])

4.5 Photon pile-up

The charge information on each CCD are read out at regular intervals, depending on the the science mode time resolution. The so-called photon pile-up occurs when the probability that more than one photon hits a pixel during a single readout cycle becomes too high. The charges released by the two photons are summed when the pixel charge is registered and the two distinct events are interpreted as one single photon with the sum of the two energies.
The main consequences which can affect the science results are an artificial hardening of the spectrum and a smaller flux of the observed source.

To avoid pileup, the flux of the source must be smaller than a particular value, which is a characteristic of each science mode. In timing mode, the flux of a point source must be smaller than 100 photons/s for the MOS camera and 800 photons/s for the pn camera (respectively corresponding to about 35 mCrab and 85 mCrab) [22].

4.6 EPIC event grade selction

Photons detected by the EPIC cameras usually land on one pixel, but some of them can also spread over a couple of pixels or more.
Every possible detection pattern is catalogued: for example a detection in one isolated pixel is a *single* event, a detection in two neighbouring pixels is a *double* event, three pixels make a *triple* event and so on.
Before the data analysis it is possible to discard from the event file certain pattern categories, which are considered suspicious: the higher the pattern identification number, the more likely is that the detection has been caused by background noise and not by a genuine X-ray.
The patterns classified as *safe* depend on the camera and the science mode.

Camera	**Mode**	**X-ray generated pattern**					**No X-ray**
		singles	doubles	triples	quadruples	higher	
MOS	imaging	**0**	**1-4**	**5-8**	**9-12**	13-25	26-31
	timing	**0**	1				2-3
pn	imaging	**0**	**1-4**	5-8	9-12		>12
	timing	**0**	**1-4**			5-12	>12

Table 4.3: The pattern catalogue. The pattern categories marked with the bold numbers are the ones recommended for the science analysis. (Source: [22])

The analysis of the pattern distribution in the event file is very helpful for evaluating the amount of photon pile-up. The genuine pattern distribution is, in fact, predicted by a model and in case of pile-up the rate of singles would decrease in favour of the doubles rate.
This happens because, with a high flux, distinct photons are more likely to fall in the same pixel and cause classical pile-up. Alternatively they could fall on two (or more) adjacent pixels and be recognised as one single photon with *double* pattern (pattern pile-up).

4.7 EPIC background

The EPIC background is due to different components:

Cosmic X-ray background: it is the actual X-ray background, coming from sources like AGN, the Local Bubble, the Galactic Disk, the Galactic Halo and from other sources located outside of the FOV, whose photons enter the telescopes with single reflection, as well as from out-of-time events (see section 4.4).

Instrumental background:

- ***Detector noise***
- ***Particle interaction:*** divided into *external flaring* and *internal quiescent background* [21].

The *EPIC external* ***flaring*** *background* is produced by soft protons (energies below some 100 keV [22]) encountered by the spacecraft, which are reflected by the telescope mirrors and funneled towards the detectors. Since this flaring background varies depending on many parameters, like the spacecraft altitude, its position in the orbit and the solar phase, it is believed that all around the Earth there are bubbles of soft protons, due to the solar activity and the Earth's magnetosphere, which works as a trap for the charged particles. The presence of the flares is unpredictable: in some measurements it can be completely absent, as it can be very strong in others [22] (the flux can be up to an order of magnitude higher than the actual source photons), in which case the entire affected measurement interval must be discarded.

The *EPIC internal* ***quiescent*** *background* is on the other hand caused by high energy particles falling on the detectors but also interacting with the stucture of the telescope.
This component is very stable with the time and has a fairly flat spectrum, threfore more influent at the higher energies. Its angular distribution is actually not homogeneous for the pn camera, in whose central region the noise is absent for some fluorescence lines. In figure 4.8 is showed the pn quiescent background at the copper line (7.8 - 8.2 keV).

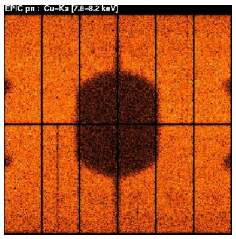

Figure 4.8: Quiescent background. (Source: [22])

The *EPIC detector noise* has multiple causes. Dark currents aren't important for the imaging modes, because they occur below 250 eV, very near to the lower energy detection threshold (100 eV), and aren't very strong. In timing mode, instead, the lower energy detection threshold is higher (200 eV) and therefore the dark currents arise at higher energies, at about 400-500 eV(a more useful energy region), and are also stronger, because a larger area on the CCD has to be selected for the data analysis [18].

In addition to this, the MOS cameras present some flickering pixels and the pn camera occasionally underestimates the energy offset for some regions of a handful of pixels, due to the high particle background. A correction for this effect on the EPIC pn camera can be performed during the data analysis, using the SAS task *epreject* [63].

4.8 Response Matrices

The sensitivity of the telescope is not uniform because the effective area varies over the energy range and over the FOV. First of all it is energy-dependent because of the mirror characteristics and the detectors (energy dependent) quantum efficiency. Then it depends also on the position in the FOV: the vignetting of the camera reduces the effective area at higher off-axis angles.
The effective area as function of the energy and the position is contained in the *ancillary response file (ARF)*.

Another file, the *redistribution matrix file (RMF)*, contains indispensable information about the energy response.
In fact, the detected photon energy is slightly different from the expected one: if a monocromatic photon beam is directed onto the detector, instead of a line, quite a broad spectrum is detected, which is usually centered on the photons' energy.

The ARF is used together with the RMF and their product is necessary during the analysis of the science data to correct for the above-mentioned effects [55][68].

4.9 The orbit

The XMM-Newton spacecraft has a very eccentric orbit with a period of about 48 h.
Due to several perturbations, the parameters of the orbit such as eccentricity, semi-major axis and inclination can vary. The orbit on the 13th July 2012 (revolution 2307) has an eccentricity $e = 0.6857$ and semi-major axis $a = 66\,939$ Km (see [20] for updates).

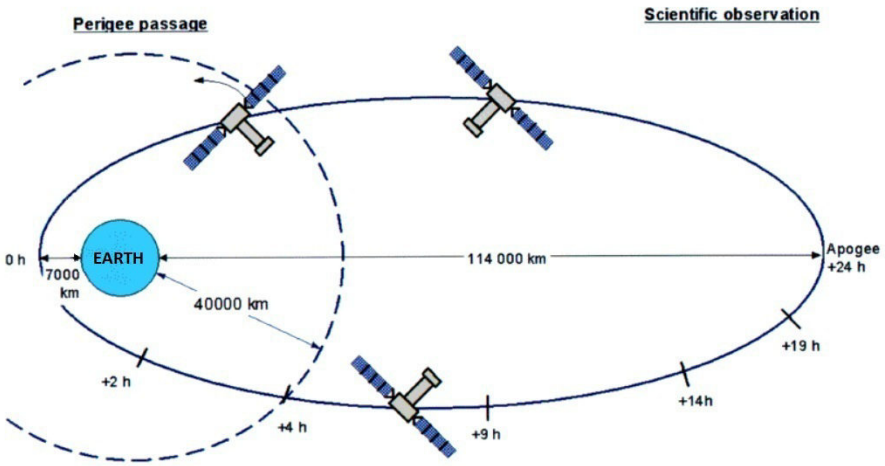

Figure 4.9: Orbit of the Telescope XMM-Newton. (Source: [22])

This eccentric orbit was chosen in order to realise long uninterrupted observations without

frequent obscurations of the Earth and to reach cool regions which allow the use of passive radiators as the only cooling system for the X-ray cameras.

The XMM-Newton cameras are operated only if the radiation background is lower than a certain threshold. A dedicated sensor constantly measures the background level, ready to shut the telescope doors and to turn the X-ray cameras off at any moment.
The telescopes never operate in the perigee region anyway, below the altitude of 46 000 Km, where the spacecraft travels through the radiation belts, whose charged particles can damage the instrumentations [12]. The perigee passage lasts about 8 hours.
Nevertheless, even at higher elevations the particle background can be very high, mainly due to the solar activity.

4.10 Barycentric correction

The raw data coming from the telescope need to be processed with the barycentric correction, which is expecially necessary for science modes with high time resolution, such as the timing mode [63].
With this correction the arrival time of each photon on the event file is modified, as if the photon had been detected at the barycenter of the Solar System [47].

XMM-Newton isn't in an inertial frame, because it orbits around the Earth and the Sun. As a consequence, photons from a source reaching the cameras must travel a longer or shorter path, depending on the position of the spacecraft in the Solar System. The time intervals between their detections are therefore different from the ones between their emissions.

The barycenter of the solar system is chosen as the reference point and is assumed to be nearly in an inertial frame. Referring to the Solar System barycenter, science measurements become comparable and, in particular, self-consistent, because during long measurements the telescope can change its position significantly.

Note that the *barycentric correction* is not the same as the *heliocentric correction*, which refers to the center of the Sun, although they are quite similar. In fact the barycenter of the Solar System lies most of the time inside of the sun.

4.11 Charge Transfer Inefficiency

Charge Transfer Inefficiency (CTI) is the imperfect transfer of charge as it is transported through the CCD during read-out [13].

A correction for the rate-dependent CTI can be performed by modifying the calibration of

the energy scale by a linear gain factor:

$$E_{original}/E_{corrected} \equiv G_{cor} = a_0 \cdot N_e^{a_i} + a_2$$

where N_e is the number of shifted electrons per pixel per second. The coefficients were estimated from previous measurements of sample sources.

This correction prevents underestimation of the energy scale for the conversion of the energy detection channel into a physical energy value.
In the overwhelming majority of the observations, after the rate-dependent CTI correction, 1.5-3 keV maximum data/model ratio is $<5\%$ [14].

Chapter 5

Analysis

Data analysis was performed with the Science Analysis System (SAS) [16] version 8.0.0, which is the main analysis tool for XMM-Newton data reduction.

The XMM-Newton observation we worked on (see paragraph 3.2) was performed in *timing mode*. The ODF (Observation Data File) available refer to the operating CCDs (see paragraph 4.4):

- **EPIC pn:** the CCD4 in timing mode;
- **EPIC MOS:** the central CCD in timing mode and the outer CCDs in standard imaging mode.

Processing the ODF with the SAS tasks *epproc* and *emproc* we produced calibrated and concatenated event lists for the EPIC cameras.

Firstly barycentric and CTI correction were performed respectively via the SAS tasks *barycen* and *epfast*. Secondly we made use of SAS to analyze the event file: we searched for possible high background periods (paragraph 5.1.1) and pile-up (paragraph 5.1.2).
We filtered subsequently the event file in the energy range, the CCD area and the pattern. We were then able to extract the tools needed for the spectral and temporal analyses from the filtered event file.

5.1 Filtering the events

5.1.1 High background periods

During observation, the telescope can go through regions in which the soft proton flaring background is very high. These intervals of flaring background can be identified by generating a light curve of high energy (E > 10 keV) single events (PATTERN=0) of the entire FOV. In fact, over 10 keV the telescope effective area is considerably smaller and the detections are dominated by non-X-ray background.
If the count rate exceeds a certain threshold, which is 0.4 cts/s and 0.35 cts/s for pn and MOS respectively, data recorded during that time interval should not be used in science analysis [13].

Using the filters:
pn: #XMMEA EP && (PI>10000) && (PI<12000) && (PATTERN==0)
MOS: #XMMEA EM && (PI>10000) && (PATTERN==0)

We found no evidence for high background periods in our data. The lightcurves of the CCDs in timing mode can be seen in figure 5.1.

5.1.2 Photon pile-up

The dedicated SAS task *epatplot* evaluates the pattern of each event and compares the ratios of singles, doubles, triples and quadruples.

The pattern distribution expected in pileup-free conditions is predicted by a model, which is plotted on a diagram together with the pattern distrubution of the event file [63]. A pattern distribution significantly different from the model is a clear sign of pileup. This usually affects restricted energy regions and the amount of singles decreases in favour of the doubles.

Epatplot also calculates the $0.5 - 2.0$ keV observed-to-model singles and doubles pattern fraction ratios, which should be consistent with 1 within the given 1-σ statistical errors. If pile-up is present, the singles ratio will be smaller than 1 and the doubles ratio will be larger than 1 [53].

We performed a pile-up analysis using the task epatplot. The test did not interest the entire FOV, but was restricted to a smaller area on the source, as the one selected in section 5.1.4 for the spectral analysis.

Epatplot diagrams of all three instruments show at low energies a very important disagreement of the pattern rates with the model and the pattern fraction ratios are different from 1, in particular for the MOS2 doubles.

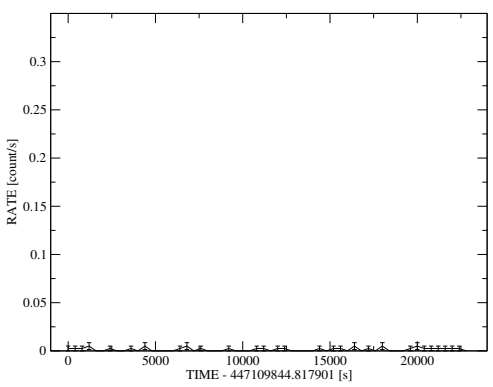

(a) *MOS1, CCD1 (timing mode).*

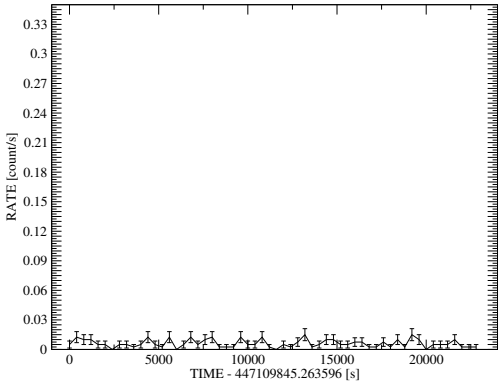

(b) *MOS2, CCD1 (timing mode).*

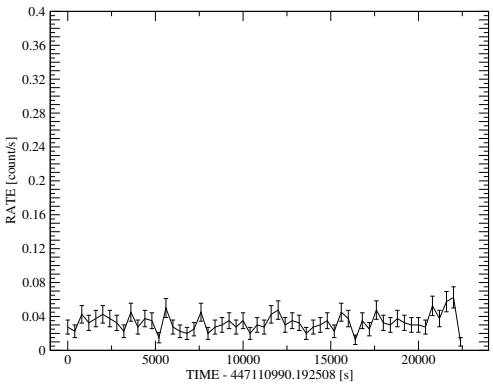

(c) *pn, CCD4 (timing mode).*

Figure 5.1: Lightcurves of the photons with energy above 10 keV. The time binsize is 400 s. A high background would be indicated by a count rate threshold of approximately 0.4 count/s and 0.35 count/s for EPIC pn and EPIC MOS respectively.
As we can see, the lightcurves display no evidence of high background periods during the observation time.

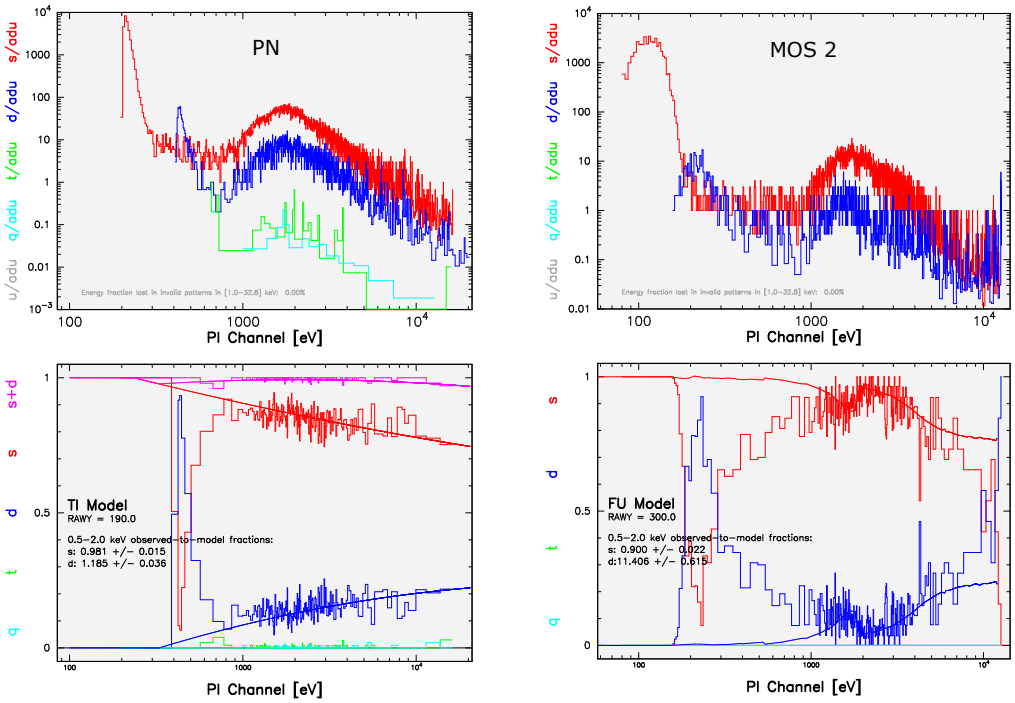

Figure 5.2: Epatplot diagrams. Left: EPIC pn CCD4. Right: EPIC MOS2 CCD1. Red, blue, green and light blue represent singles, doubles, triples and quadruples respectively. On the upper panels the number of events is plotted. On the lower panel one can see the ratio of the number of events of each pattern over the total together with the model curve.

Considering the EPIC pn camera, we can observe in the upper panel two peaks at energies of about 210 eV and 420 eV. In the lower panel the rates of singles and doubles deviate remarkably from the model at 420 eV, the higher of the two peak energies.
This feature is caused by electronic noise, which becomes relevant in timing mode measurements [18]. The electronic noise occurs in single events, observed as the 210 eV peak. Its remarkable intensity causes pattern-pileup, which produces a peak of double events at 410 eV.

A similar behaviour is shown by the MOS1 and MOS2 cameras, where the peak of singles appears at about 120 eV and 85 eV respectively.

EPIC pn patterns agree with the models on the remaining energy range.
EPIC MOS patterns, instead, are discordant at high energies. Nevertheless, this is not a genuine sign of pile-up and the discrepancy is uniquely due to scarce statistics in the high energy range. In fact, the flux of the source is far below the flux limit for pile-up for the MOS cameras [22]. Even in previous measurements no pile-up had been encountered for this source, although they had been performed in imaging mode and therefore much more likely to be affected by pile-up.
In conclusion we found no evidence of pile-up.

Only events in the energy range in which the observed pattern distribution agrees with the model should be considered for further science analysis [18]. The standard energy selection above 500 eV for EPIC pn and above 300 eV for EPIC MOS seems to be not enough. In fact, the pile-up test was repeated after the standard filtering and the pattern rates were still in disagreement with the model.
Only an energy selection above 800 eV could restore the accordance of the pattern distributions with the theory in all three detectors.

5.1.3 Energy and event grade selections

We filtered our eventfile energies, keeping only those events with energy between 800 eV and 10 keV. We rejected data above 10 keV because in this range we have poor statistics and the detections are dominated by soft proton flares.

The event grade was restricted to singles for the MOS cameras (PATTERN==0) and both singles and doubles for the pn camera (PATTERN<=4), as suggested in the Users Guide to SAS for the spectral analysis of eventfiles obtained in timing mode [63].
Also the selection FLAG==0 is recommended.

5.1.4 EPIC pn angular selections

After the filtering of the event files, angular selections for source and background were chosen.

Pn CCD4 is composed of a grid of 64x200 pixels. During a timing mode measurement, photons are collected on the entire CCD surface. Any information as to their y position is immediately lost, because all photon events associated to the same column are integrated in one pixel.
Each time integration yields, therefore, a 64-pixel stripe, in which the only spatial information about the source is the x position.
The subsequent measurement stripes are then stored along the original y column.
By measuring a compact source, we obtain a measurement containing a central bright stripe, which shows the evolution of the source over time.

The observed compact source XMMU J173203.3-344518 lies in the center of the CCD4 x-axis, as can be seen in figure 5.3. The *source* selection must contain all detections of the complete observation interval and is therefore enclosed in a long stripe. The source selection is displayed in figure 5.4.

The EPIC pn *background* was also chosen on the CCD4. We selected two regions on both sides of the source with equal area and distance from the source (see figure 5.4), as suggested in the Users Guide to SAS [63].

We registered a discrepancy between the spectra extracted from the left and the right side of the background selection. In particular, the spectrum from selection on the left (A) has a flux of about 70% higher than the one on the right (B).

We exclude that a contribution from the surrounding SNR HESS J1731-347 may have influenced the background regions near the source. In fact, looking at the morphology of the remnant, as it was detected by XMM during the measurement of March 2007 (see table 3.1), we can identify a large circular bright feature on the left, therefore near the B region, rather than the A region.

We hypothesize that this asymmetry might be produced by internal noise, perhaps linked to the readout process.
We compared our results with another measurement, which investigated the bright X-ray binary Her X-1. The pn CCD4 in timing mode background in the 0.8-10 keV band is about 70% stronger on the left than on the right.

In conclusion we decided to use both the left and the right selection together as background, in order to obtain a balanced background spectrum. In fact, considering its central position,

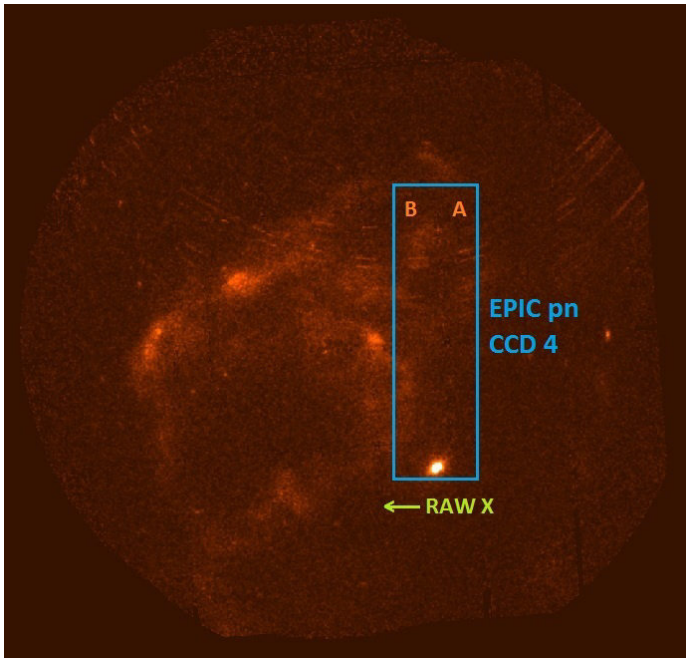

Figure 5.3: Image of the SNR HESS J1731-347 containing our source. This picture was obtained from the XMM-Newton measurement of March 2007. The square represents the region covered by the pn CCD4 of the new measurement, performed in timing mode.

we expect the source to be associated with a background averaged between left and right background.

This idea is also supported by the results of the further spectral analysis. The model fitting yields the best results when the background is extracted from both A and B region, rather than from just one of the two selections.

5.1.5 EPIC MOS angular selections

Such as the pn CCD4, the MOS CCD1 is performed in timing mode. The entire CCD is composed of a grid of 600x600 pixels, but in timing mode only a central area of 100x600 pixels is active. Similarly as for pn CCD4, during the measurement photons collected on the same stripe are integrated in one pixel. Also in this case the measurement of a compact source contains a central bright stripe.

The *source* selections for MOS1 and MOS2 interest the approximately central region of the respective CCD1, as shown in figure 5.5.

Due to the impact of a micreometeoroid in 2005, as explained in section 4.3.1, MOS1 CCD1 is affected by a hot line very close to the boresight, which has to be excluded [13]. The source selection is, therefore, centered on the source but composed by two narrow stripes

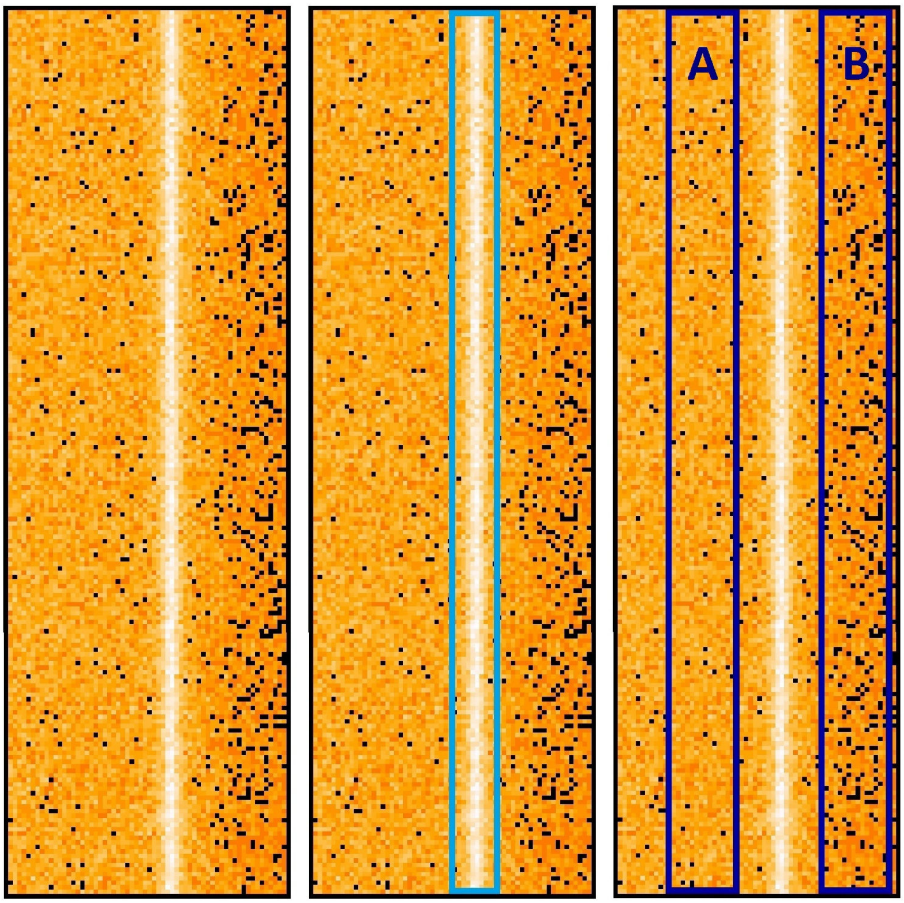

Figure 5.4: EPIC pn angular selections. Each panel plots the angular parameter RAWY as function of RAWX. RAWY position gives information on the arrival time of each detection. Events registered during a certain readout are associated to a particular RAWY. After the maximum value RAWY = 200 is associated to the events of the 200th readout cycle, the following set of events wil be associated again to the first value RAWY = 1 and so on. In fact, the number of readouts performed during the total measurement time is far higher than the number of pixels along the RAWY axis of the CCD.
Left: the measurement from the pn CCD4. Middle: the source selection (light blue). Right: the background selection (blue), composed of the A and the B region.

on both sides of the hot line.
Such an important exicision close to the source causes a significant loss in the photons coming from the source.

The MOS *background* should not be selected on the central CCD on the sides of the source region, because the CCD is only 100 pixels wide. A background with better statistics can be obtained from the outer CCDs, operated in imaging mode [63].

Our initial background selections can be seen in figure 5.6.

Our source, however, is located in an X-ray emitting supernova remnant and the background can vary significantly from region to region. A background extracted from the outer CCDs, and therefore so far away from the source, can be misleading.
It is also important to remember that measurements obtained in different modes are differenlty affected by instrumental background. Subtracting a background spectrum obtained in imaging mode from a source spectrum obtained in timing mode can thus be inappropriate.

We could confirm this statement as we started performing spectral analysis on our data using this background. None of the adopted models (description and motivation of which can be found in section 5.2.1) yielded a good chi squared. High residuals are present at both high and low energies, as can be seen in some spectrum plots in figure 5.7.

As the standard background selection procedure was not successful, we decided to exctract a new background from the central CCD. Although the remaining area available on the CCD was limited and the statistics consequently poor, the new background selection yielded much better spectral fits of the source spectrum.

The new background selections for MOS are displayed in figure 5.5.

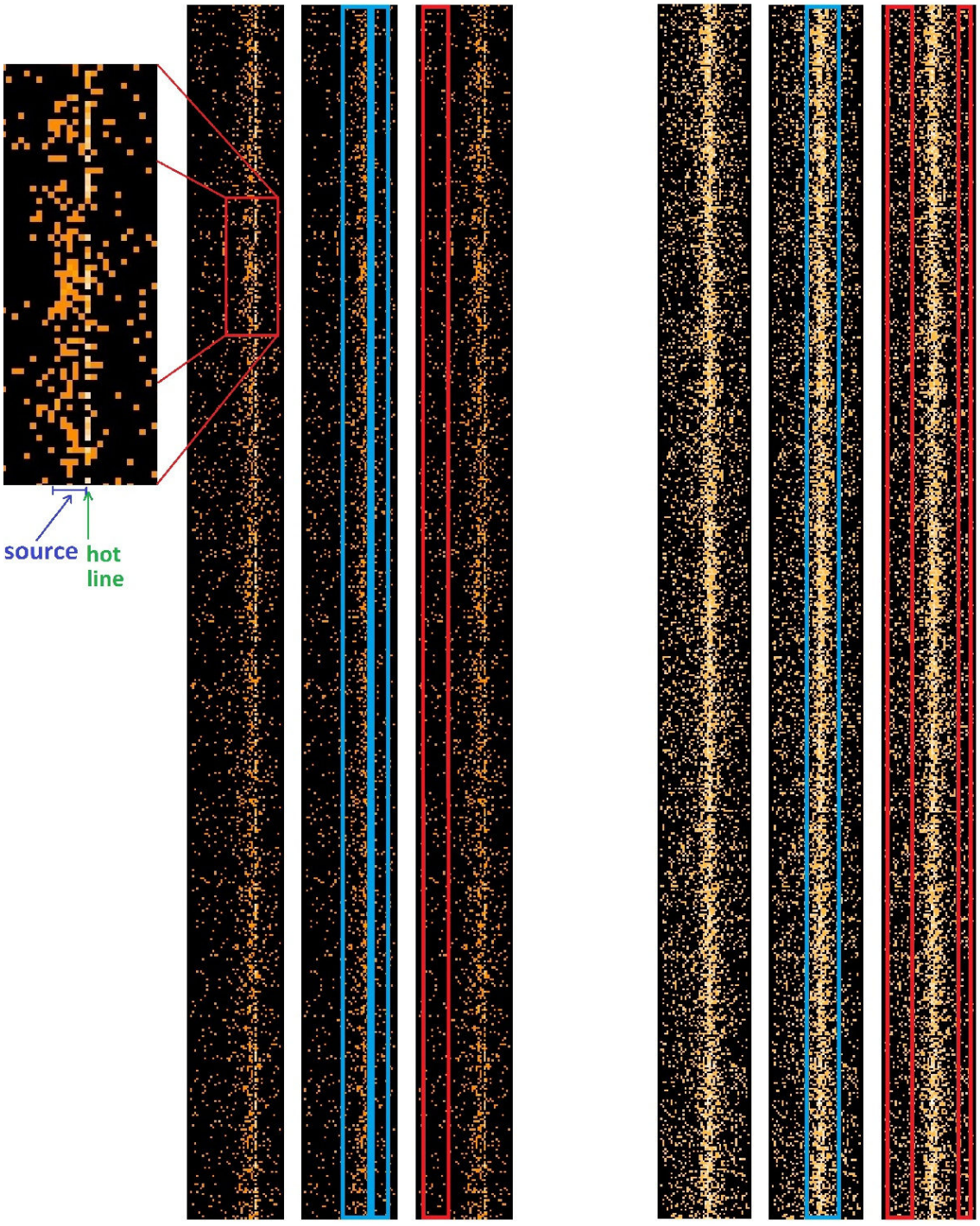

Figure 5.5: EPIC MOS angular selections. Each panel plots time as function of the angular parameter RAWX. Left: the measurement from the MOS1 CCD1, the source selection (light blue) and the definitive background selection (red). At the top left an enlargement shows the hot line, which had to be excluded from the MOS1 source angular selection. Right: the measurement from the MOS2 CCD1, the source selection (light blue) and the definitive background selection (red).
Note that the background selections were eventually chosen on the same CCD as the source selections, even though not suggested in the Users Guide [63].

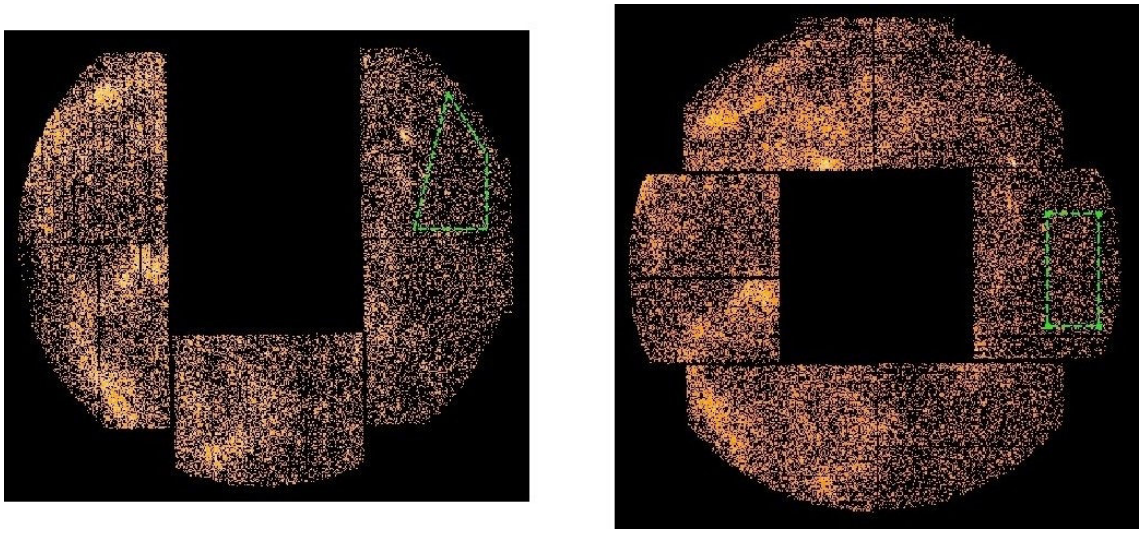

Figure 5.6: Background selections from the outer CCDs of MOS1 (left) and MOS2 (right) cameras are defined by the green dotted lines.

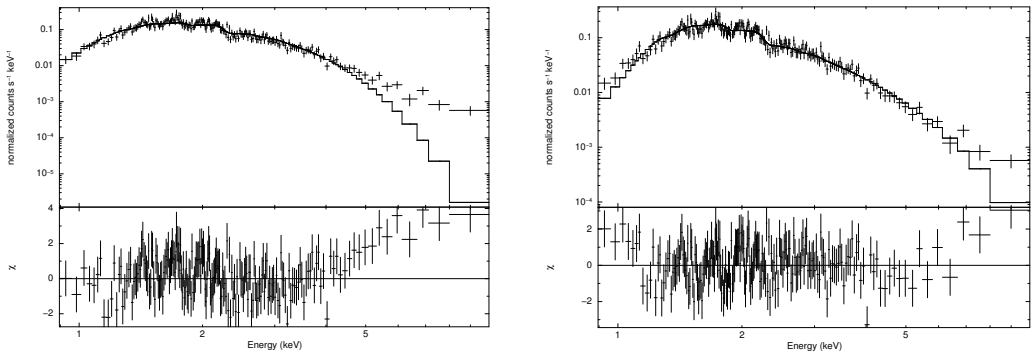

Figure 5.7: Spectral fits for the MOS2 data using the initial background selection from the outer CCDs. Blackbody (left) and powerlaw (right) fits.

As the fit of the source spectrum together with the outer background selection spectrum yielded bad chi squared for all the adopted models, we preferred to choose a background selection on the CCD1 (see picture 5.5).

5.2 Spectral analysis

Spectral analysis was perfomed using *xspec*.
For the analysis of each dataset we need a spectrum of the source and possibly a spectrum of the background. Two other files are indispensable: the ancillary response file (ARF) and the redistribution matrix file (RMF), as explained in section 4.8. They are calculated with SAS on the particular source angular selection.

We encoutered some problems with the ARF for the MOS1 source selection. In fact, its calculation requires that spectral extraction regions are symmetric. This is not our case, for we had to excise a hot line from the source selection. The appropriate ARF for MOS1 was calculated from three ARFs of symmetric regions similar to the source region, which were then subtracted as explained in one of the SAS watchout pages [54].

The datasets were then loaded and fitted with different spectral models.

5.2.1 Fit models and motivations

Following the current literature on CCO and magnetar, four different models were investigated, in order to confirm or reject the one or the other possibility.
The spectral models we adopted are summarized in table 5.1.

model	model description	command	free parameters
(a)	absorbed blackbody	cflux*wabs*bbody	k_BT, n_H, Flux, N_b
(b)	absorbed powerlaw	cflux*wabs*powerlaw	α, n_H, Flux, N_p
(c)	absorbed blackbody + powerlaw	cflux*wabs(bbody+powerlaw)	k_BT, α, n_H, Flux, N_b, N_p
(d)	absorbed two blackbody	cflux*wabs(bbody+bbody)	k_BT_1, k_BT_2, n_H, Flux, N_{b1}, N_{b2}

Table 5.1: Models used for our spectral fits [69].

bbody	is a blackbody spectrum with distribution $A(E) = \frac{N_b\, 8.05251\, E^2\, dE}{(k_B T)^4 \left(\exp\left(\frac{E}{k_B T}\right) - 1\right)}$ $k_B T$ is the temperature in keV, $N_b = \frac{L_{39}}{D_{10}^2}$ is the normalisation, L_{39} is the source luminosity in units of $10^{39} ergs^{-1}$, D_{10} is the distance to the source in units of 10 kpc.
powerlaw	is a simple power law with distribution $A(E) = N_p E^{-\alpha}$ α is the photon index of powerlaw, N_p is the normalisation, in $photons\, keV^{-1} cm^{-2} s^{-1}$ at 1 keV.
wabs	is a photo-electric absorption using Wisconsin cross-sections [46] $M(E) = exp\,(-n_H \sigma(E))$ $\sigma(E)$ is the photo-electric cross-section, n_H is the equivalent hydrogen column (in units of $10^{22}\, atoms\, cm^{-2}$).
cflux	is a convolution model to calculate the flux of other model components. We fixed the minimum energy to 800 eV and the maximum energy to 10 keV. The only free parameter is log10Flux, which yields the log(base10) of the flux, in $ergcm^{-2} s^{-1}$.

The model *cflux* is only a device to calculate the flux and doesn't substantially bring any physical meaning to the model. The model *wabs* represents the absorption of the emission by the physical environment located between the source and the telescope. The third component of the model is what actually describes the physical properties of the source.

(a) Blackbody is the typical model for CCO emission, in which photons are most likely radiated from the hot surface [11]. Also magnetars can produce a pure blackbody emission. Even robust evidence for a blackbody spectrum would, therefore, not be sufficient to characterize the nature of XMMU J173203.3-344518.

(b) Power law emission is produced in non-thermal processes, which usually occur in the star magnetosphere or in a possible pulsar wind nebula.

(c) Blackbody associated with power law emission has also been registered in magnetars as a combination of both thermal radiation from the surface and non-thermal radiation from the magnetosphere.

(d) A two blackbody spectrum could describe the thermal emission from a hot surface, which is in addition being heated in restricted areas (like the poles) by high energy particles.

5.2.2 Fit results

The datesets of the three EPIC cameras were fitted togheter with the above-mentioned models. The best fit parameters in the spectral anlysis are reported together with the 90% confidence interval errors. Figure 5.8 contains the four spectra with the fitted model curves. In the lower panel of each chart the residuals to the model are also displayed.

The fit statistic results and the model best-fit parameters are listed in table 5.2.

	blackbody	**powerlaw**	**blackbody+ powerlaw**	**two blackbody**
$\overline{\chi^2}$	1.082	1.299	1.072	1.072
d.o.f	761	761	759	759
n.h.p	$6 \cdot 10^{-2}$	$5 \cdot 10^{-8}$	$8 \cdot 10^{-2}$	$8 \cdot 10^{-2}$
$n_H\,(10^{22} cm^{-2})$	1.55 ± 0.07	3.5 ± 0.1	$1.8\ ^{+0.4}_{-0.3}$	1.6 ± 0.1
photon index	-	4.8 ± 0.1	$3\ ^{+2}_{-3}$	-
$k_B T_1\,(keV)$	0.489 ± 0.009	-	0.47 ± 0.02	$0.46\ ^{+0.02}_{-0.07}$
$k_B T_2\,(keV)$	-	-	-	$0.9\ ^{+2}_{-0.3}$
$\text{flux}_{[0.5-10keV]}\,(10^{-12})$	2.37 ± 0.04	$2.49\ ^{+0.4}_{-0.5}$	$2.43\ ^{+0.06}_{-0.05}$	$2.41\ ^{+0.07}_{-0.05}$

Table 5.2: Best-fit parameters of the spectral analysis.

The power law model is rejected, as it yields a high chi squared and a very small related null hypothesis probability. We reject, therefore, the possibility of a pure power law emission from the source.

Blackbody model, conversely, represents a very good fit for our data.
An slightly better chi squared is obtained by the two composite models. Nevertheless, we cannot immediately conclude that the composite models fit our data better than the single blackbody model. In fact, composite models have more free parameters and can therefore more easily match the data distribution.
To check if the addition of a component to the blackbody model represents a considerble advantage to the goodness of the fit, we performed an F-test using the xspec task *ftest*. We obtained for both models an F-ratio of 3.7, which corresponds to a p-value of about 2.6%,

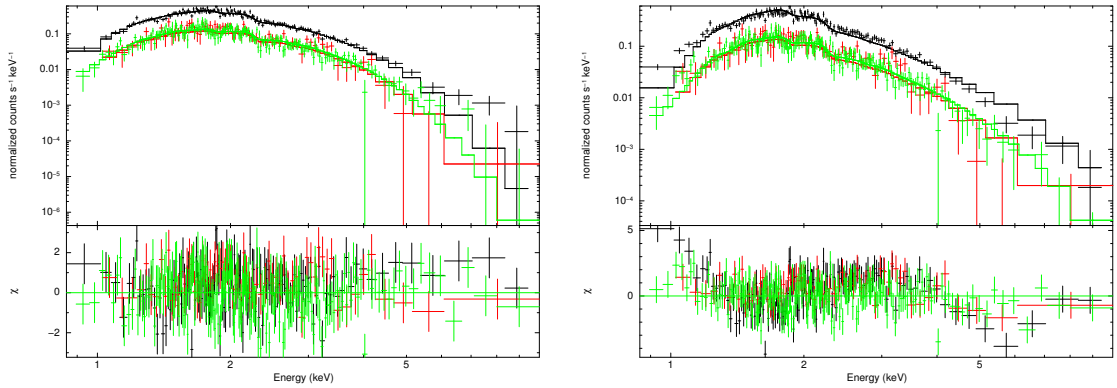

(a) *Blackbody*

(b) *Power law*

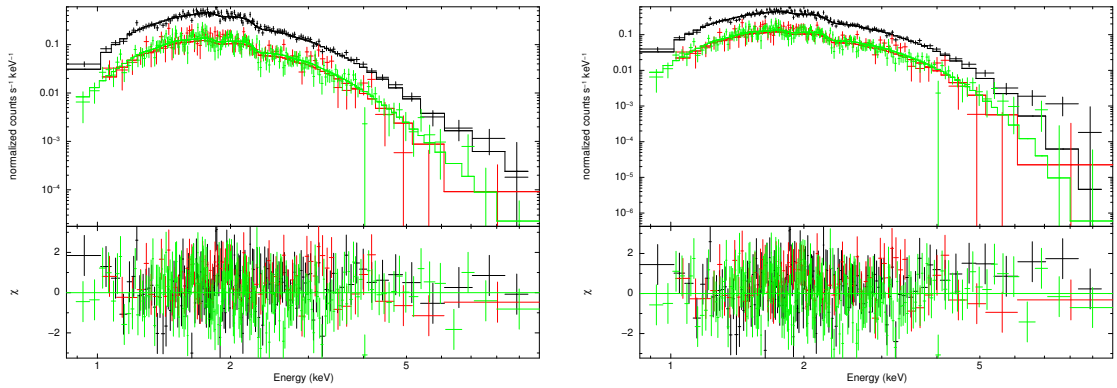

(c) *Blackbody plus power law*

(d) *Two blackbody*

Figure 5.8: The spectrum of pn (black), MOS1 (red) and MOS2 (green) together, fitted with different models. In the lower box the residuals are plotted, i.e. the deviation of the data from the model.

which is not enough for supporting one of the composite models rather than the simple blackbody.

We then compared the best-fit parameters from our data with the ones obtainened in the previous analysis of the source. The absorption column density, the effective temperature and the flux are shown in figure 5.9, 5.10 and 5.11 respectively.

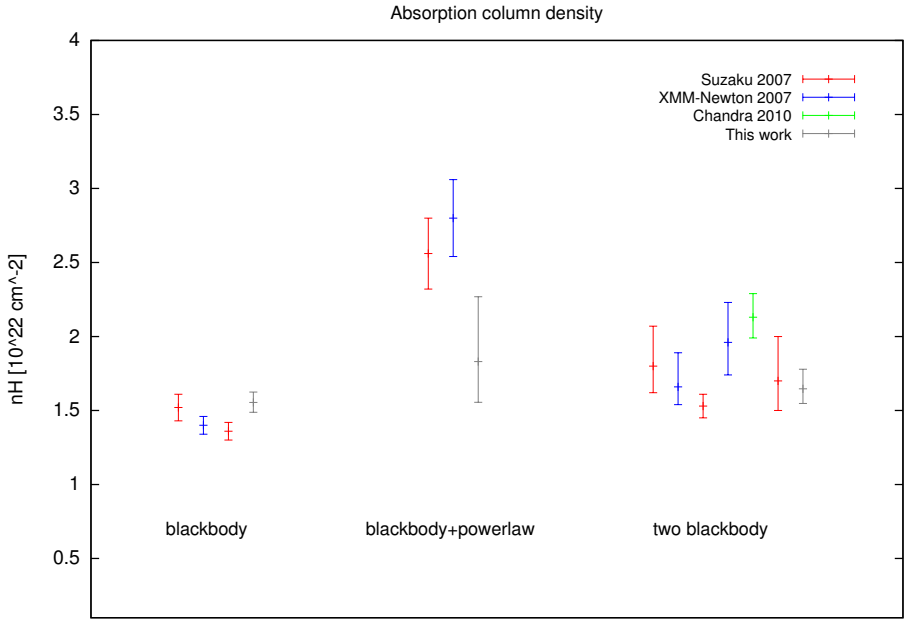

Figure 5.9: Absorption colum density (parameter of *wabs*). The previous analyses of Suzaku, XMM-Newton and Chandra here displayed were perfomed by [27], [61], [28] and [4].

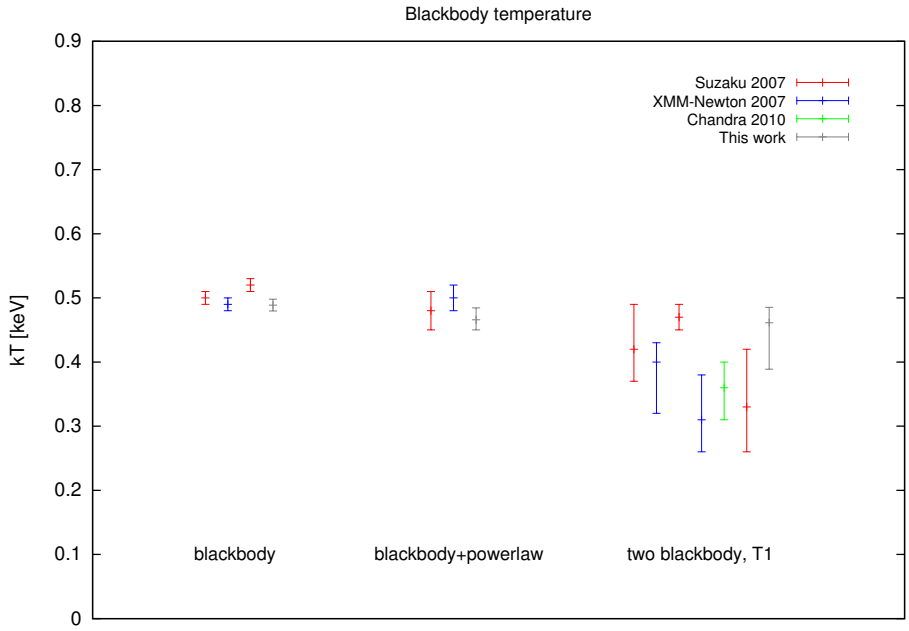

Figure 5.10: Effective temperature (parameter of *bbody*). The previous analysis data refer to [27], [61], [28] and [4].

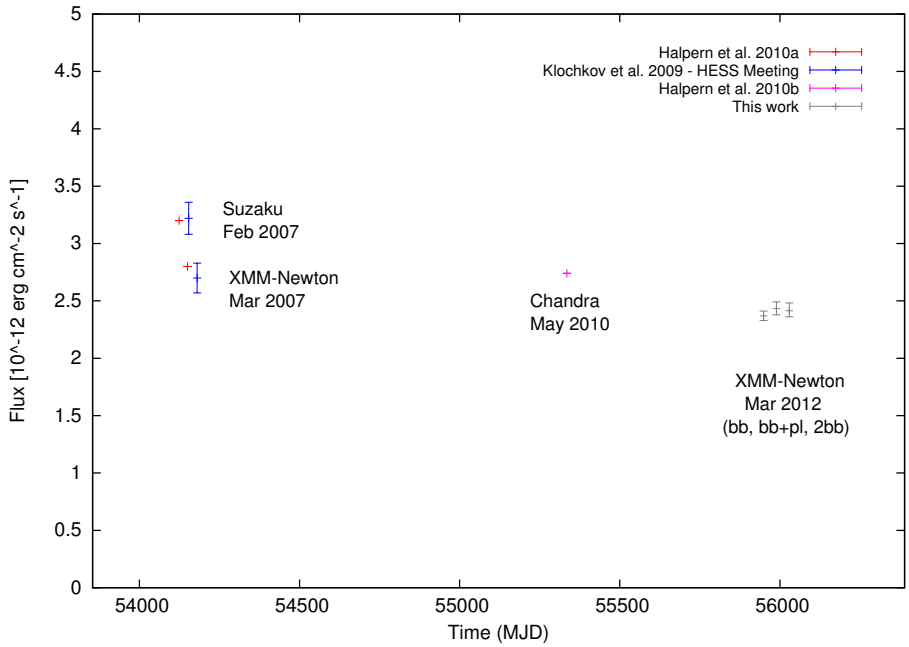

Figure 5.11: Flux of the spectrum (parameter of cflux) as function of the Modified Julian Date (MJD). All fluxes refer to the 0.5-10 keV energy range, except of *Klochkov et al. 2009*, which refers to the 0.6-10 keV energy range. *Halpern et al. 2010a* and *Klochkov et al. 2009* time values overlap each other and have been slightly shifted in this plot. The same was done for the three values of our analysis.

5.3 Timing analysis

The analysis of the temporal evolution of the source emission was carried out in two resolution scales.
A low-resolution lightcurve can reveal long term flux modulations or flares. A high time resolution lightcurve is investigated to search for periodic pulsations of the emission.

5.3.1 Low-resolution lightcurves

A lightcurve was extracted with a rough resolution, in order to investigate possible variations of flux with time. These variations could be a flux increase or decrease tendency over a long time. Even sudden strong flares, which could be evidence for magnetar activity [5], can not be excluded.
The lightcurves of the three detectors are separately plotted in figure 5.12.

No significant variation was found in the low-resolution lightcurves. The counts per second are approximately constant. The slight scattering displayed in figure 5.12 is consistent with the errorbars.
No flaring activity was detected during the time span of our observation.

5.3.2 Search for pulsations

Pulsations of the source emission were searched by performing a Fast Fourier Transform (FFT) of the high time resolution lightcurve. The transform was carried out on the event-files from only the EPIC pn camera using the ftool *powspec* [48].

5.3.3 The Fourier transform

In general, the Fourier transform describes a given function as a sum of sine waves.
Each sine wave frequency is associated with a certain amplitude and the Fourier transform displays the spectrum of those amplitudes.

Not only continuous, but also discrete functions can be Fourier transformed.

The *continuous Fourier transform* decomposes an infinitely extended continuous funciton into an inifinite number of sine waves [64].

$$a(\nu) = \int_{-\infty}^{+\infty} x(t) e^{i\,2\pi\nu t} dt \qquad -\infty < \nu < +\infty$$

$$x(t) = \int_{-\infty}^{+\infty} s(\nu) e^{-i\,2\pi\nu t} d\nu \qquad -\infty < t < +\infty$$

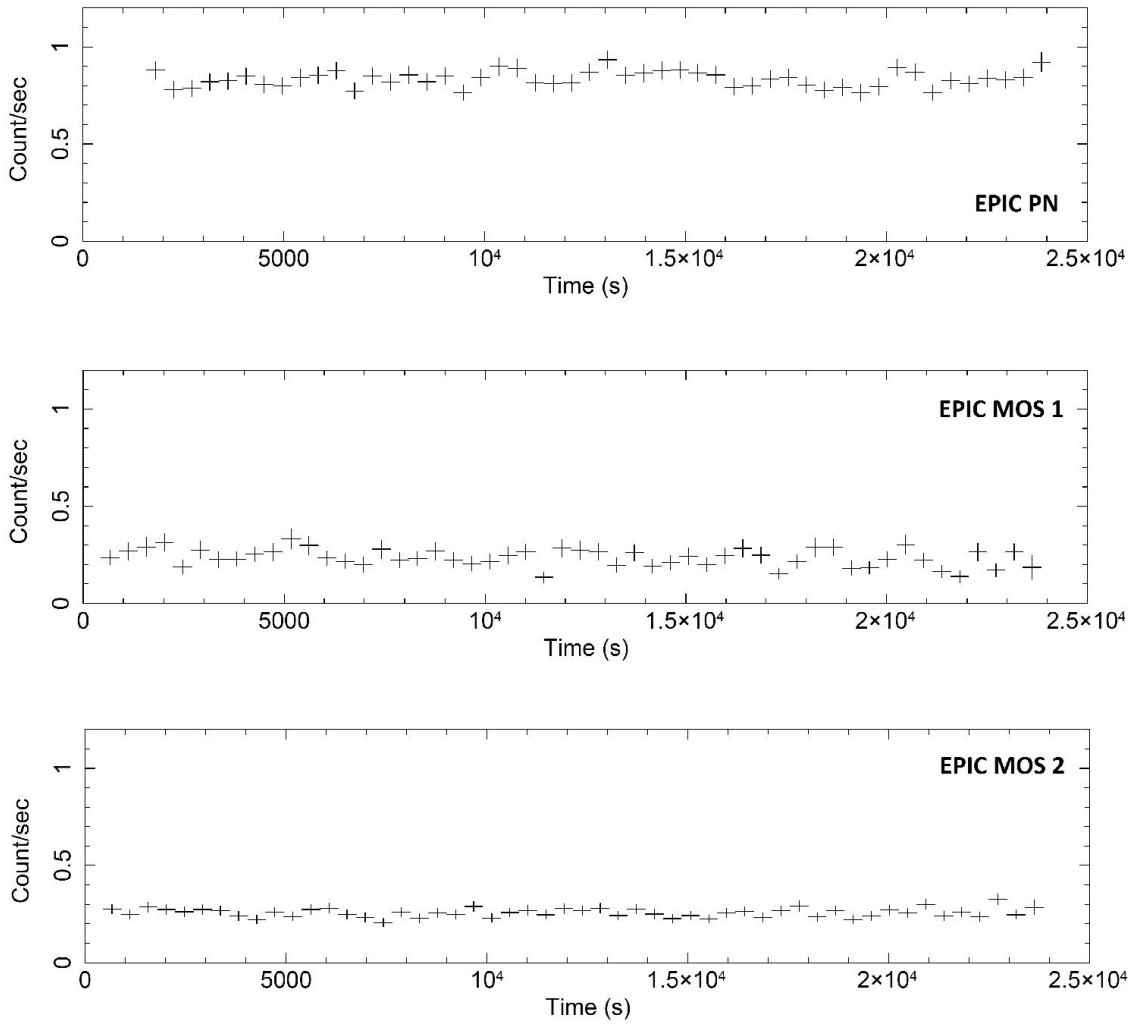

Figure 5.12: Lightcurves of the three detectors with time resolution 450 s. The displayed errorbars are the statistical errors calculated with 90% confidence.

where $a(\nu)$ is the Fourier frequency spectrum and $x(t)$ the initial function of time.

The *discrete Fourier transform* applies, conversely, to a discrete function of a finite domain, therefore over a finite time interval T.

$$a_j = \sum_k x_k \, e^{i\,2\pi\nu_j t_k} \qquad\qquad j = -\frac{N}{2}, \dots, \frac{N}{2}$$
$$x_k = \frac{1}{N} \sum_j a_j \, e^{-i\,2\pi\nu_j t_k} \qquad\qquad j = 0, \dots, N-1$$

where a_j are the discrete values of the Fourier frequency spectrum and x_k the discrete values of the initial function. The Fourier power spectrum is the spectrum of the $|a_j|^2$, the squared module of the complex Fourier amplitudes a_j.

If the continuous Fourier transform of a sine wave is simply a delta function, the same is not valid for a discrete Fourier transform of a sine wave defined over an enclosed domain. In fact, the *domain limitation* and the *sampling* of the initial function bring important modifications in the resulting frequency spectrum.

The main effect of a domain limitation is a broadening of the power spectrum features to a width of 1/T, where T is the time length of the original function.
A sampling of the input function, on the other hand, modifies the power spectrum by periodically repeating the expected features, at frequency intervals of N/T, where N is the number of values of the original function. This phenomenon is also known as aliasing.
As a result, a discrete function is completely described using the discrete Fourier transform by a finite number of frequencies, comprised between 0 and $\nu_{N/2} = \frac{1}{2}N/T$, the so-called *Nyquist frequency* [64].

Scientific data can have neither infinite length nor be continuous, therefore the discrete Fourier transform is used in scientific signal analysis.
The Fast Fourier Transform (FFT), which was used in our analysis, is a particular algorithm which implements a discrete Fourier transform and produces a frequency spectrum in a finite number of bins.

5.3.4 Signal detection

The frequency spectrum bins obtained with FFT contain mainly noise, but may also contain a signal interesting for scientific analysis.
To give evidence for the detection of a signal against a noise background we firstly need knowledge of all the probability distribution of the noise powers.

5.3.5 The noise power distribution

The noise fluctuations are generally governed by the Poisson statistic and therefore follow a chi-squared distribution with 2 degrees of freedom [64]. Under this condition, the probability that the noise power $P_{j,noise}$ in a certain bin of the frequency spectrum exceeds a threshold P_T is:

$$Prob(P_{j,noise} > P_T) = \int_{P_T}^{\infty} \chi_n^2(P)dP = \int_{P_T}^{\infty} e^{-\frac{P}{2}}dP$$

$$\chi_n^2(t) = \left[2^{\frac{n}{2}-1}\Gamma\left(\frac{n}{2}\right)\right]^{-1} t^{\frac{n}{2}-1}e^{-\frac{t}{2}}$$

where $\chi_n^2(P)$ is the chi-squared distribution with n degrees of freedom [64][65].

The $\chi_2^2(P)$ distribution has a mean value of 2 and a variance of 4.
In order to reduce the large variance, two methods can be applied [64].

- prior to the FFT, the lightcurve is divided into M equal intervals, to which is applied the FFT separately; the M produced frequency spectra are then averaged into one single spectrum
- after the FFT, the frequency spectrum is rebinned, averaging W consecutive bins.

Both methods degrade the frequency resolution, but bring a significant reduction of the variance of the noise distribution, as can be seen in figure 5.13. In fact the noise power then follows the chi-squared distribution with 2MW degrees of freedom $\chi_{2MW}^2(P)$, which has a variance of 4/MW.
Nevertheless, this procedure is not suggested for the detection of a narrow feature from a strictly sinosoidal signal [64], as in our case.
The signal power $P_{j,signal}$ of a narrow feature drops as $\sim \frac{1}{MW}$. Therefore, our search was performed over the entire lightcurve length ($M = 1$) and with no averaging ($W = 1$), to assure the best sensitivity.

5.3.6 The total power distribution

Not only noise, but also signal may be contained in the bins of the frequency spectrum.
In a given bin j, the total power $P_{j,tot}$ results from the interaction of noise power $P_{j,noise}$ and signal power $P_{j,sig}$.

If the value of MW is relatively large we can assume the additivity of noise and signal powers $P_{tot} = P_{noise} + P_{sig}$. For a given P_{sig}, the distribution of the P_{tot} is therefore exclusively

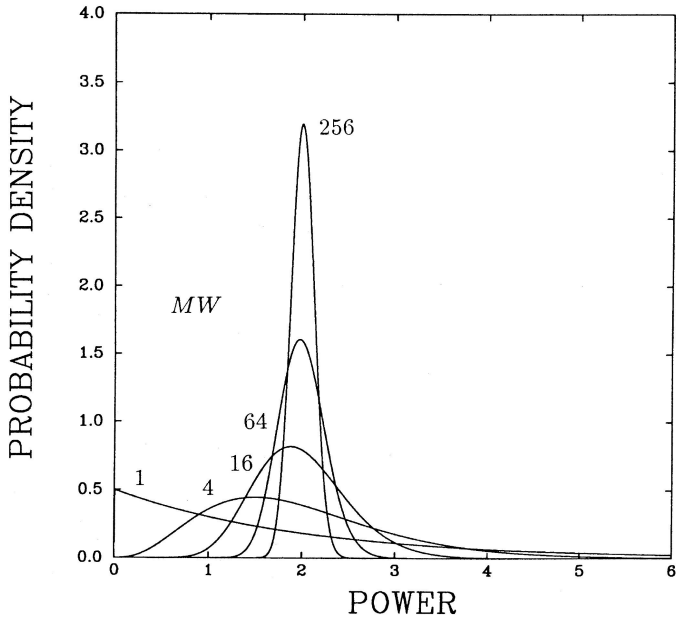

Figure 5.13: The probability distribution of average noise powers for different values of the number of powers MW averaged. The distributions are equivalent to the chi-squared distribution with 2MW degrees of freedom. (Source: [64])

ruled by the noise statistics and is similar to a chi-squared statistics with power values shifted by a P_{sig} amount.

$$Prob(P_{tot} > P_T) = \int_{P_T}^{\infty} \chi^2_{2MW}(P - P_{sig})dP \qquad P > P_{sig}$$

However, when MW is relatively small the additivity assumption is incorrect and P_{tot} follows a distribution different than the one described above. The probability that P_{tot} exceeds a certain power P_T is:

$$f_{MW}(P_T; P_{sig}) = Prob(P_{tot} > P_T) =$$

$$= \int_{P_T}^{\infty} \left(\frac{P}{P_{sig}}\right)^{\frac{(MW-1)}{2}} e^{-\frac{(P+P_{sig})}{2}} I_{(MW-1)}[(PP_{sig})^{\frac{1}{2}}]\, dP =$$

$$= e^{-\frac{(P_T+P_{sig})}{2}} \sum_{m=0}^{\infty} \sum_{k=0}^{m+MW-1} P_T^k P_{sig}^m \,/\, \left(k!\, m!\, 2^{m+k}\right)$$

where I is a modified Bessel function of the first kind [65].
For a given confidence probability value of f_{MW}, we calculate the value of P_{sig} from the maximal observed total power P_T. Another option for the calculation of P_{sig} is the use

of the probability contours given by Groth (1975) [26] displayed in figure 5.14 (note that Groth's power normalisation is a half of ours.

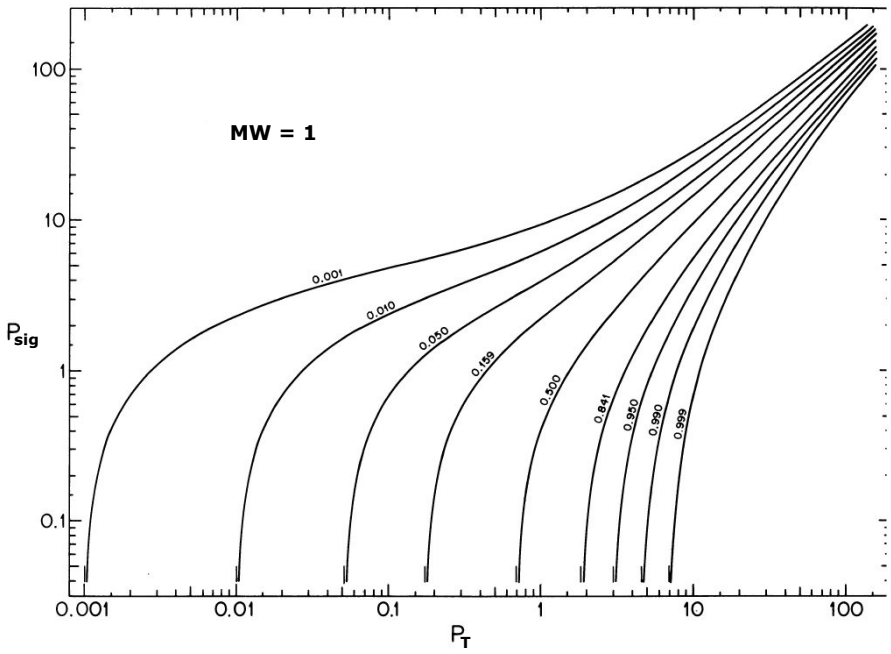

Figure 5.14: Percentage points of the distribution of $Prob(P_{tot} > P_{_T})$ versus P_T and P_{sig} for MW=1. (Source: [26])

5.3.7 The detection level

The detection level establishes how large the power of a possible detection must be in order to represent a genuine excess to the noise [64].
The C-confidence level P_{detect} is the power with 1-C probability to be exceeded by one of the powers in the frequency spectrum, assuming that only noise is present in the power distribution [65]:

$$1 - C = N_{trial}\ f_{_{MW}}(P_{detect}; P_{sig})$$

where N_{trial} is the number of independent bins considered. C is usually a large probability number, for example 0.9 or 0.99.

If a $P_{j,tot}$ happens to exceed the detection level P_{detect}, there is a large C probability that it contains not only noise, but also genuine signal [64].

5.3.8 The detection of a sinusoidal shape

The *upper limit amplitude* is calculated from the signal power $P_{j,sig}$ of the bin j containing P_{max} and a given shape of the signal one wishes to detect.
The customary choice is to refer to a sinusoidal pulse shape.

In this section we calculate the signal power $P_{j,sig}$ detected in the frequency bin j and produced by a sine wave of a given amplitude A, frequency ν_{sine} and phase ϕ.
The sinusoidal profile

$$x_k = 1 + A\sin(\omega_{sine}\, t_k + \phi)$$

is transformed by the FFT into the frequency spectrum:

$$|a_j|^2 = \left(\frac{AN_\gamma}{2}\right)^2 \left(\frac{\sin(\pi x)}{\pi x}\right)^2 \left[\left(\frac{\pi x/N_\gamma}{\sin(\pi x/N_\gamma)}\right)^2 + \left(\frac{\pi x/N_\gamma}{\sin[\pi(2j+x)/N_\gamma]}\right)^2 + \right.$$
$$\left. + 2\left(\frac{\pi x/N_\gamma}{\sin(\pi x/N)}\right)\left(\frac{\pi x/N_\gamma}{\sin[\pi(2j+x)/N]}\right)\cos[(N_\gamma - 1)(2\pi(j+x)/N_\gamma) + 2\phi]\right]$$

where N_γ is the total number of photons and $x = (\nu_{sine} - \nu_j)T$ is the frequency offset of the bin frequency to the sinusoid frequency.
For frequency bins close to ν_{sine} ($x/N \ll 1$) and not too close to zero or the Nyquist frequency ($0 \ll j/N \ll \frac{1}{2}$) the frequency spectrum reduces to:

$$|a_j|^2 \approx \left(\frac{AN_\gamma}{2}\right)^2 \left(\frac{\sin(\pi x)}{\pi x}\right)^2$$

The corresponding signal power $P_{j,sig}$, according to the adopted normalisation, is [65]:

$$P_{j,sig} = \frac{1}{MW}\frac{2}{N_\gamma}|a_j|^2 \approx \frac{A^2 N_\gamma}{2MW}\left(\frac{\sin(\pi x)}{\pi x}\right)^2$$

Note that the coefficient $\frac{1}{MW}$ describes the reduction of the detected power in the search for a narrow feature, when MW bins are averaged according to section 5.3.5.

We can average the behaviour of the sinc function over the posible frequency offsets x in one bin, obtaining [65][64]:

$$< P_{j,sig} > \approx 0.773\,\frac{A^2 N_\gamma}{2MW}\,\mathrm{sinc}^2\left(\frac{\pi}{2}\frac{\nu_j}{\nu_{nyquist}}\right)$$

So we eventually obtain, inverting the previous equation, a relation between the power in the frequency spectrum and the amplitude of modulation of the transformed signal:

$$A \approx 1.61\sqrt{\frac{MW\, P_{j,sig}}{N_\gamma}}\left[\mathrm{sinc}\left(\frac{\pi}{2}\frac{\nu_j}{\nu_{nyquist}}\right)\right]^{-1}$$

The value of A calculated using the value of $P_{j,sig}$ from the bin containing P_{max} (see section 5.3.6 is the upper limit amplitude A_{UL} for sinusoidal profile.

5.3.9 Our measurements

We performed a period search on the EPIC pn data, which have much better statistics compared to MOS1 and MOS2. The lightcurve has a length of $T \approx 22445.64$ s and bin resolution $\Delta T_{bin} \approx 2.68$ ms. The number of bins of the lightcurve was therefore $n_{bin} = T/\Delta T_{bin} = 8388608$.

The time bin is chosen to be much larger than the timing resolution of EPIC PN to avoid numerical problems with FFT calculation, because of insufficient memory capacity of our computers. ΔT_{bin} is close to the theoretical limit of neutron star rotation period.

Further analysis of the data will be performed in future using the Rayleigh periodgram, also known as the Z_1^2-statistics [50]. This approach requires a smaller amount of computer memory and therefore will allow us to perform period search with a better time resolution.

In order to achieve the best sensitivity to coherent pulsations, the FFT was performed over the entire time interval T of the lightcurve (M=1) and the frequency spectrum was not rebinned (W=1).

In the power spectrum, the Nyquist frequency was $\nu_{nyquist} = n_{bin}/(2T) = 186.86$ Hz and the frequency resolution $\Delta\nu_{bin} = 1/T = 4.46 \cdot 10^{-5}$ Hz.
The number of frequency bins, i.e. the number of trials is $N_{trial} = \nu_{nyquist}/\Delta\nu_{bin} = 4194304$.

The detection threshold with 99% confidence level is $P_{detect} = 39.7$.
No signal is detected above the 99% *confidence level threshold*, as none of the bins contain a P_{tot} higher than P_{detect}. The maximum registered total power is $P_{max} = 31.24$.
The power distribution in our power spectrum is displayed together with the theoretical noise power distribution in figure 5.15.

The signal power calculated in the bin with maximum power P_{max}, taking into account the interpretation between P_{sig} and P_{noise} [65] is $P_{sig} = 61.47$. The corresponding 99% confidence upper limit on the amplitude for frequencies far from the Nyquist frequency $\nu_{nyquist}$ is $A_{UL} \approx 9\%$, assuming a sinusoidal pulse shape.

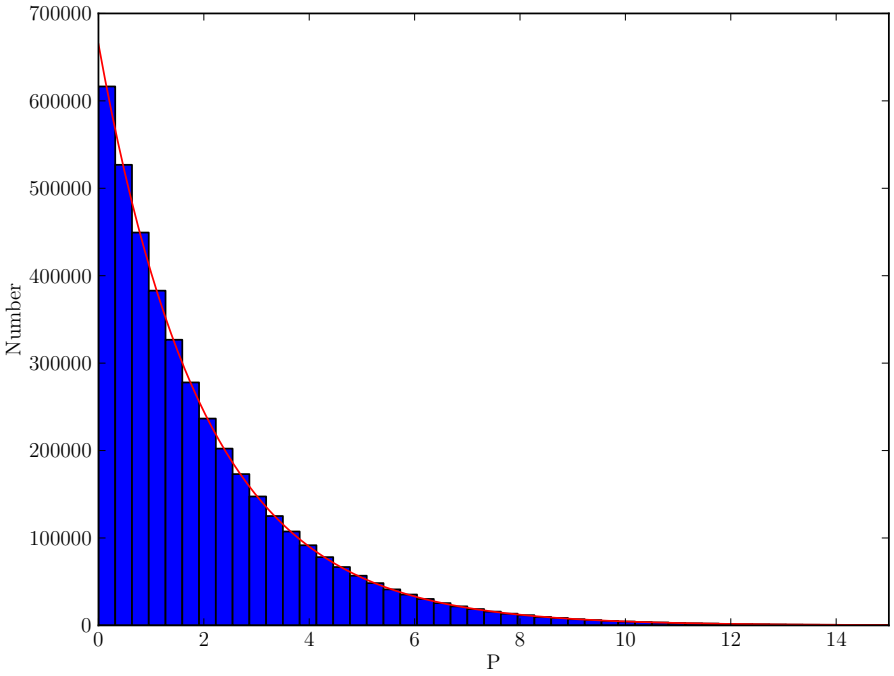

Figure 5.15: Power distribution histogram in our power spectrum. The red curve is the theorical renormalised probability-density function of noise powers.

Chapter 6

Conclusions and outlook

We analyzed the data of the XMM-Newton observation of the source performed on march 2012.

For the spectral analysis all three X-ray instruments (PN, MOS1 and MOS2) were used. The spectra in the 0.8-10 keV energy range are well described by an absorbed blackbody model with effective temperature $k_BT = 0.489(9)$ keV. We found no evidence for an additional powerlaw component, although it could not be ruled out.

The new flux measurement indicates a few sigma lower flux compared to that previously measured with Suzaku, Chandra and XMM-Newton. It cannot be excluded, however, that the systematic differences in the instrument response in different observing modes (timing and imaging) and the systematic uncertainties in the absolute flux calibration (for XMM-Newton it is believed to be around 10% [15]) are responsible for the observed differences in flux. We conclude, therefore, that these differences are not sufficient to claim a long-term variability of the source.

Low-resolution lighcurves from our measurements did not reveal any significant variations in a shorter time scale either.
Our results tend to favour the CCO scenario, rather than the AXP hypothesis.

The search for pulsations was carried out only on the data from the pn camera and did not reveal the presence of pulsations down to 5.36 ms. The absence of pulsations, or their weakness, is compatible with a blackbody emission radiated from nearly the entire surface of the neutron star.

From the unabsorbed flux and the temperature of the blackbody spectrum model, a constraint on the ratio between radius of the emission surface R and distance of the neutron star D can be calculated (see section 2.6).

Considering the radius in km and the distance in 10 kpc, it was estimated:

$$\frac{R_{[km]}}{D_{[10kpc]}} \approx 11.3$$

Under the assumption that the CCO is located either in the Scutum-Crux arm (~ 3.0 kpc) or in the Norma-Cygnus arm (~ 4.5 kpc) [30], the radius of the emitting area is estimated to be 1 km and 1.5 km respectively. These values of R are much smaller than the typical size of a neutron star of about 10 km and such a system is expected to produce some pulsation.

Only at a distance of at least $D \sim 30$ kpc the emission radius would be $R \sim 10$ km and therefore compatible with the absence of pulsations. However, this solution is not plausible. At such a large distance the TeV emission from the associated SNR would be exceedingly high and its radius would be $r_{SNR} \sim 260$ pc, whereas the other TeV shell SNRs have radius smaller than 15 pc [30].

A similar problem is reported for the CCO in Cas A and solved by fitting the power spectrum with a carbon atmosphere model [34].
Hydrogen in the thin atmosphere of a neutron star can undergo nuclear processes on the hot surface and be transformed in other heavier elements such as carbon [10].

We are currently working on the fit of the XMMU J173203.3-344518 observation performed with XMM-Newton in 2007 in imaging mode. The source spectrum is fitted using a carbon atmosphere model developed in our group.

The fit yields good chi squared for the source at both distances of 3.2 kpc and 4.5 kpc. The effective temperature is $T \sim 2.5 \cdot 10^6$ K.

The spectrum of the source XMMU J173203.3-344518 is therefore compatible with that of a more or less isotropically emitting neutron star with a carbon atmosphere at a distance of 3-4 kpc.

Chapter 7

Summary

In this thesis we report our analysis of the XMM-Newton observations of the CCO candidate XMMU J173203.3-344518.

The source had already been investigated before and best-fit models to the spectrum were consistent with an absorbed blackbody spectrum component with effective temperature $k_BT \sim 0.5$ keV. No flux modulation had been reported over a time span of three years and no pulsation of the source had been detected. It was not possible to conclude whether the star was a CCO or an AXP, as the observed characteristics are consistent with of both classes.

Our analysis of the new dataset was aimed at a search for pulsations of the source and of possible flux variations, which would help to determine the source classification.

The best fit of the spectra from all three instruments (pn, MOS1 and MOS2) in the 0.8-10 keV energy range is given by an absorbed blackbody model with effective temperature $k_BT = 0.489(9)$ keV. Considering systematic differences in the instrument response in different observing modes (timing and imaging) and the systematic uncertainties in the absolute flux calibration between different telescopes, we found no evidence of flux variation over a time span of 5 years.

The pn data did not reveal pulsations and yield a 99% confidence upper limit on the pulsed fraction of a sinusoidal signal of 9% for any for any period down to 5.36 ms.
These characteristics tend to favour the CCO scenario, rather than the AXP hypothesis.

The absence of pulsations could be explained by an emission radiated from nearly the entire surface of the CCO. Assuming a distance of 3-4 kpc, the area of emission calculated from the fit parameters is, however, much smaller.
A solution to this puzzle is perhaps a carbon atmosphere, following [34]. The spectrum of the source observed by XMM-Newton in 2007 is in fact well described by a carbon atmosphere model with effective temperature of about 0.2 keV. The area of the emission

estimated with this model is of the order of the CCO surface area and this would explain the absence of pulsations. The spectrum of the source XMMU J173203.3-344518 is therefore compatible with that of a more or less isotropically emitting neutron star with a carbon atmosphere.

Chapter 8

Zusammenfassung

In dieser Diplomarbeit wird die Analyse der XMM-Newton Beobachtung der CCO Kandidat XMMU J173203.3-344518 beschrieben.

Die Quelle wurde schon früher untersucht und best-fit Modelle für das Spektrum sind kompatibel mit einem arbsorbierten Schwarzkörper mit Schwarzkörpertemperatur $k_BT \sim 0.5$ keV. Es wurde keine Flussänderung über eine Zeitspanne von ungefähr drei Jahre registriert und keine Pulsation der Quelle detektiert. Es war unmöglich zu unterscheiden, ob die Quelle ein CCO oder ein AXP ist, weil solche Charakteristiken kompatibel mit Objekten beider Klassen sind.

Das Ziel unserer Analyse war die Suche nach Pulsationen der Quelle und nach möglichen Flussänderungen, die unsere Quelle schließlich klassifizieren würden.

Das best-fit aller Spektren aus den dreien Instrumenten (pn, MOS1 and MOS2) über dem Energiebereich 0.8-10 keV ist ein absorbierter Schwarzkürper mit Effektivtemperatur $k_BT = 0.489(9)$ keV. Der Fluss stimmt mit den vorherigen Messungen überein, wenn man systematische Unterschiede zwischen Aufnahmemoden und systematische Unsicherheiten in der Flusskalibrierung zwischen verschiedenen Teleskopen berücksichtigt. Es wird deshalb von uns angenommen, dass der Fluss konstant über eine Zeitspanne von 5 Jahre ist.

Keine Pulsation wurde in den pn Data erkannt und die 99% Konfidenzintervall Obergrenze auf dem gepulstem Bruchteil eines sinusförmigen Signals ist 9% für perioden bis 5.36 ms. Diese Eigenschaften sind eher charakteristisch für CCOs als AXP und deswegen lehnen wir die AXP Hypothese ab.

Die Abwesenheit von Pulsationen könnte von einer Emission aus der ganzen Oberfläche des CCOs verursacht werden. Die Emissionsfläche ist aber viel kleiner, wenn man den Abstand von 3-4 kpc annimmt.
Eine Lösung für dieses Rätsel ist vielleicht ein Kohlenstoff Atmosphärenmodell, wie bei [34]. Das spektrum der Quelle aus der XMM-Newton Beobachtung von 2007 ist gut von

einem Kohlenstoffatmosphärenmodell mit Effektivtemperatur 0.2 keV beschrieben.
Die mit disem Modell geschätzte Emissionsoberfläche ist ungefähr so groß wie die Sternoberfläche und das würde die Pulsationsabwesenheit erklären. Das Spektrum der Quelle XMMU J173203.3-344518 ist deshalb kompatibel mit dem von einem mehr oder weniger isotropisch emittierenden Neutronenstern mit einer Kohlenstoffatmosphäre.

Chapter 9

Acknowledgements

I would like to express my sincere gratitude to Andrea Santangelo for giving me the possibility to work with the Tübingen HEA research group. My thanks must go in particular to Dmitri Klochkov and Gerd Pühlhofer for the constant supervision and the patience in answering all my questions.

A special thanks goes to my family, Dan and all my friends.
Without their support and encouragement, this study would have not been possible.

Bibliography

[1] Acero F., Pühlhofer G., Klochkov D., Komin Nu., Gallant Y., Horns D., Santangelo A., for the H.E.S.S. Collaboration (2009) Proceedings of the 31st ICRC, *X- and gamma-ray studies of HESS J1731-347 coincident with a newly discovered SNR*, arXiv:0907.0642

[2] Aghaei-Khozani H., *X-Ray Telescope Design Principles and Abundance Targets*, http://www.mpa-garching.mpg.de/lectures/ADSEM/SS09_Aghaei.pdf

[3] ATNF pulsar catalogue, http://www.atnf.csiro.au/people/pulsar/psrcat/

[4] Bamba A. et al. (2012) ApJ 756 149, *Suzaku observations of the non-thermal supernova remnant HESS J1731-347*, arXiv:1207.4182

[5] Becker W., *Neutron Stars and Pulsars*, Springer (2009), ISBN-13 9783540769644

[6] Brazier K., Johnston S. (1999) MNRAS 305 (3): 671-679, *The implications of radio-quiet neutron stars*, arXiv:astro-ph/9803176

[7] Central Compact Objects in SNRs, http://hera.ph1.uni-koeln.de/~heintzma/NeutronStar/CCO.htm

[8] Chamel N. and Haensel P. (2008), Living Rev. Relativity 11, 10, *Physics of Neutron Star Crusts* arXiv:0812.3955v1

[9] Chandra X-ray Observatory, ACIS Instrument information, http://cxc.harvard.edu/cal/Acis/

[10] Chandra X-ray Observatory, *Carbon Atmosphere Discovered On Neutron Star*, http://chandra.harvard.edu/press/09_releases/press_110409.html

[11] De Luca A. (2008) AIP Conf. Proc. 983, pp. 311-319, *Central Compact Objects in Supernova Remnants*,
arXiv:0712.2209

[12] ESA Science and technology, XMM-Newton,
http://sci.esa.int/science-e/www/area/index.cfm?fareaid=23

[13] ESA XMM-Newton Calibration Documentation, EPIC status of calibration and data analysis (Jul 2012),
http://xmm2.esac.esa.int/docs/documents/CAL-TN-0018.pdf

[14] ESA XMM-Newton Calibration Documentation, Evaluation of the spectral calibration accuracy in EPIC-pn fast modes (Nov 2012),
http://xmm2.esac.esa.int/docs/documents/CAL-TN-0083.pdf

[15] ESA XMM-Newton Calibration Documentation, Status of XMM-Newton instrument cross-calibration with SAS v10.0,
http://xmm2.esac.esa.int/docs/documents/CAL-TN-0052.ps.gz

[16] ESA XMM-Newton Data Analysis,
http://xmm.esa.int/sas/

[17] ESA XMM-Newton EPIC MOS1 CCD6 Update,
http://xmm.esac.esa.int/external/xmm_news/items/MOS1-CCD6/index.shtml#20050630

[18] ESA XMM-Newton Helpdesk, issue EPICpn/7644,
http://xmm2.esac.esa.int/xmmhelp/EPICpn?id=7644;page=2;user=guest

[19] ESA XMM-Newton Introduction to SAS,
http://xmm.esa.int/sas/current/documentation/sas_concise.shtml

[20] ESA XMM-Newton Orbit and Constraints Details,
http://xmm2.esac.esa.int/external/xmm_sched/vischeck/orbit_details.shtml

[21] ESA XMM-Newton Science Operation Centre - A Technical Description,
http://xmm.esac.esa.int/external/xmm_user_support/documentation/technical/

[22] ESA XMM-Newton Users Handbook - Issue 2.10,
http://xmm.esac.esa.int/external/xmm_user_support/documentation/uhb/XMM_UHB.pdf

[23] Fitzpatrick R., *Quantum Mechanics: An intermediate level course*,
http://farside.ph.utexas.edu/teaching/qmech/lectures/node65.html

[24] Goddard Space Flight Center, Swift Response Matrices,
http://heasarc.gsfc.nasa.gov/docs/swift/proposals/swift_responses.html

[25] Gotthelf E., Halpern J. (2009) ApJ 695 L35, *Discovery of a 112 ms X-ray Pulsar in Puppis A: Further Evidence of Neutron Stars Weakly Magnetized at Birth*,
arXiv:0902.3007

[26] Groth E. (1975) ApJS 286, 29:285-302, *Probability distributions related to power spectra*,
doi:10.1086/190343

[27] Halpern J.P. and Gotthelf E.V. (2010a) ApJ 710 941, *Two magnetar candidates in HESS supernova remnants*,
arXiv:0912.4985

[28] Halpern J.P. and Gotthelf E.V. (2010b) ApJ 725 1384, *An energetic magnetar in HESS J1713-381/CTB 37B*,
arXiv:1008.2558

[29] Heger et al. (2003) ApJ 591 288, *How Massive Single Stars End Their Life*,
doi:10.1086/375341

[30] HESS Collaboration, Abramowski et al. (2011) A&A 531, A81, *A new SNR with TeV shell-type morphology: HESS J1731-347*,
arXiv:1105.3206

[31] H.E.S.S. Source of the Month (mar 2009), *HESS J1731-347 - an old supernova remnant?*,
http://www.mpi-hd.mpg.de/hfm/HESS/pages/home/som/2009/03/

[32] H.E.S.S. Source of the Month (oct 2010), *A new SNR shell resolved in TeV gamma rays*,
http://www.mpi-hd.mpg.de/hfm/HESS/pages/home/som/2010/10/

[33] Hinton J.A., Hofmann W. (2009) Ann.Rev.Astron.Astrophys.47:523-565, *Teraelectronvolt Astronomy*,
arXiv:1006.5210

[34] Ho W., Heinke C. (2009) Nature 462, 71-73, *A neutron star with a carbon atmosphere in the Cassiopeia A supernova remnant*,
arXiv:0911.0672

[35] Ikhsanov N., Kim V., Beskrovnaya N., Pustil'nik L. (2013) arXiv preprint, *On the origin of the 6.67 hr period pulsar 1E 161348-5055*,
arXiv:1212.0375

[36] Jansen F. et al. (2001) A&A 365, L1-L6, *XMM-Newton Observatory - I. The Spacecraft and Operations*,
doi:10.1051/0004-6361:20000036

[37] Kaspi V., Roberts M., Harding A. (2004) Cambridge Astrophysics Series, No. 39, *Isolated Neutron Stars*,
arXiv:astro-ph/0402136

[38] Kirk J. G., Lyubarsky Y., Petri J. (2007) Astrophysics and Space Science Library 357, 421-450, *The theory of pulsar winds and nebulae*,
arXiv:astro-ph/0703116

[39] Klochkov D. (2010) XMM-Newton Proposal ID #06739301, *A central compact object in the center of a new supernova remnant shell?*,
XMM-Newton Proposal ID 06739301

[40] Leahy et al. (1983) ApJ 266 160, *On searches for pulsed emission with application to four globular cluster X-ray sources - NGC 1851, 6441, 6624, and 6712*,
doi:10.1086/160766

[41] Longair M., *High Energy Astrophysics*, Chambridge University Press (2001), ISBN-13 9780521756181

[42] Lumb D. H. et al. (1991) Experimental astronomy 2:179-201, *Charge Coupled Devices (CCDs) in X-ray Astronomy*,
http://btc.montana.edu/ceres/malcolm/cd/universe/assets/multimedia/ccd.pdf

[43] McGill SGR/AXP Online Catalog,
http://www.physics.mcgill.ca/~pulsar/magnetar/main.html

[44] Medin Z., Lai D. (2010) MNRAS 406 (2): 1379-1404 , *Pair cascades in the magnetospheres of strongly-magnetized neutron stars*,
arXiv:1001.2365

[45] Meyer R., Pavlov G., Meszaros P. (1994) ApJ 433 265, *Soft X-ray spectral FITS of Geminga with model neutron star atmospheres*,
doi:10.1086/174642

[46] Morrison, R., McCammon, D. (1983) ApJ 270 119, *Interstellar photoelectric absorption cross sections, 0.03-10 keV*,
doi:10.1086/161102

[47] NASA Fermi Science Support Center, *Barycentric Correction*
http://fermi.gsfc.nasa.gov/ssc/data/analysis/documentation/Cicerone/Cicerone_Pulsars/barycentric_correction.html

[48] NASA's heasarch - Xronos powspec,
http://heasarc.gsfc.nasa.gov/xanadu/xronos/examples/powspec.html

[49] Pavlov G., Sanwal D., Teter M. (2003) arXiv preprint, *Central Compact Objects in Supernova Remnants*,
arXiv:astro-ph/0311526

[50] Protheroe R.J. (1987) Proc. ASA 7 (2), *Periodic analysis of gamma-ray data*,
http://adsabs.harvard.edu/full/1987PASAu...7..167P

[51] Russeil D., Adami C. and Georgelin Y. M. (2007) A&A 470, 161-171, *Revised distances of Northern HII regions*,
doi:10.1051/0004-6361:20066051

[52] Sangwook P. et al. (2008) ApJ 695 431, *Nonthermal X-Rays from Supernova Remnant G330.2+1.0 and the Characteristics of its Central Compact Object*,
arXiv:0809.4281

[53] SAS Threads, *How to evaluate the pile-up fraction in an EPIC source*,
http://xmm.esac.esa.int/sas/current/documentation/threads/epatplot.shtml

[54] SAS watchout page - *I heard that one column in MOS1 Timing Mode is affected by "high offset": can I still analyze the data?*,
http://xmm.esa.int/sas/current/watchout/Evergreen_tips_and_tricks/mos1_timing.shtml

[55] Saxton R. (2012), *EPIC Detector Matrices*,
http://xmm.vilspa.esa.es/external/xmm_sw_cal/sas_workshop/sas_ws7_files/day01/08_detmat_talk_saswk6.pdf

[56] Shapiro S., Teukolsky S., *Black holes, white dwarfs and neutron stars: The Physics of Compact Objects*, Wiley-VCH (1983),
ISBN-13 9780471873167

[57] SPIE Digital Library, Optical Engineering,
http://opticalengineering.spiedigitallibrary.org/article.aspx?articleid=1183211

[58] TeVCat, online Gamma-ray catalog,
http://tevcat.uchicago.edu/

[59] The H.E.S.S. Source Catalog,
http://www.mpi-hd.mpg.de/hfm/HESS/pages/home/sources/

[60] Tian W.W., Leahy D.A., Haverkorn M., Jiang B. (2008) ApJ 679 L85, *Discovery of the radio and X-ray counterpart of the TeV gamma-ray source HESS J1731-347*,
arXiv:0801.3254

[61] Tian W.W., Li Z., Leahy D.A., Yang J., Yang X.J., Yamazaki R., and Lu D. (2010) ApJ 712 790, *X-ray emission from HESS J1731-347/SNR G353.6-0.7 and central*

compact source XMMS J173203-344518,
arXiv:0907.1684

[62] Tian W.W., Leahy D.A. (2010) arXiv preprint, *Radio and X-ray observations of Five TeV SNRs*,
arXiv:1010.0217

[63] Users Guide to the XMM-Newton Science Analysis System - Issue 9.0,
http://xmm.esac.esa.int/external/xmm_user_support/documentation/sas_usg/USG/

[64] Van der Klis M. (1988) Proceedings of the NATO Advanced Study Institute Timing Neutron Stars, Çes,me, Turkey, 4-15 April 1988, NATO ASI Series C, Vol. 262, *Fourier techniques in X-ray timing*,
http://dare.uva.nl/document/45712

[65] Vaughan et al. (1994) ApJ 435 362, *Searches for millisecond pulsations in low-mass X-ray binaries, 2*,
doi:10.1086/174818

[66] VHE γ-ray Sky Map and Source Catalog,
http://www.mppmu.mpg.de/~rwagner/sources/index.html

[67] XMM-Newton EPIC Background Components,
http://www.star.le.ac.uk/~amr30/BG/BGTable.html

[68] XMM-Newton Data Center at MPE, Response Files for EPIC pn and EPIC MOS,
http://www.mpe.mpg.de/xray/wave/xmm/cookbook/EPIC_PN/spectral/response.php#ARF

[69] XSPEC V12 Models,
http://heasarc.gsfc.nasa.gov/docs/xanadu/xspec/manual/XspecModels.html